Joule heating synthesis of NiFe alloy/MoO$_2$ and in-situ transformed (Ni,Fe)OOH/MoO$_2$ heterostructure as effective complementary electrocatalysts for overall splitting in alkaline seawater

Zhan Zhao [a], Jianpeng Sun [a], Xiang Li [a], Zisheng Zhang [b], Xiangchao Meng [a],[*]

[a] Key Laboratory of Marine Chemistry Theory and Technology (Ministry of Education), College of Chemistry & Chemical Engineering, Ocean University of China, Qingdao, Shandong, 266100, China
[b] Department of Chemical and Biological Engineering, Faculty of Engineering, University of Ottawa, Ottawa, Ontario, K1N6N5 Canada

ABSTRACT

Designing highly-efficient and stable bifunctional seawater splitting electrocatalyst is fascinating, but still face challenges. Guided by unique interfacial properties within heterostructures, we herein reported on a rapid Joule heating method to integrate NiFe alloy on surface of MoO$_2$ as a bifunctional electrocatalyst for seawater splitting. Benefited from the synergistic effects at interfaces of NiFe alloy/MoO$_2$ (denoted as FeMoNi/NF), as-prepared samples exhibited Pt similar HER activity (20 mV @ 10 mA cm^{-2}) in alkaline seawater. Moreover, surface reconstruction could occur on NiFe alloy to generate active (Ni,Fe)OOH/MoO$_2$ heterojunction under OER conditions, which achieved superior activity (250 mV @ 50 mA cm^{-2}) in alkaline seawater. Notably, with the rapid Joule heating, the FeMoNi/NF showed face-centered cubic phase for Fe$_{0.5}$Ni$_{0.5}$ alloy, which could further modulate the Fe-Ni bonds, improve electrical conductivity and provide more oxygen defects, thus causing better electrochemical properties than FeMoNi/NF-C (synthesized by conventional method). Of particular note, the extremely low cell voltage (1.45 V @ 10 mA cm^{-2}) without IR compensation was obtained for practical membrane electrode assembly (MEA) electrochemical reactor. In addition, with the introduction of FeMoNi/NF, corresponding high solar-to-hydrogen (STH) conversion efficiency is up to 12.47 % for photovoltaic (PV)-assisted water electrolysis system under simulated sun (AM 1.5-G 100 mW·cm^{-2}) illumination. DFT calculations demonstrated the synergetic interactions at the interfaces of alloy-metal oxides as well as the mechanistic research on catalytic sites towards HER/OER.

1. Introduction

Hydrogen (H$_2$) has been considered as a promising alternative for conventional fossil fuels, which can be generated by electrocatalytic water splitting [1–5]. Unfortunately, even if the low water demand for direct purity water electrolysis (~9.01 kg H$_2$O per 1 kg H$_2$), the growing demand of Net zero Emissions Scenario will lead to considerable consumption of freshwater resources [6]. Meanwhile, one of the challenging barriers for water electrolysis are the existence of increasing water pollution and population crisis, which leads to freshwater scarcity and restricts the hydrogen industrialization due to the extra-costs [7,8]. In terms of that, the introduction of seawater into the electrocatalytic system has been the forefront of research and promising strategy, wherein the seawater is nearly inexhaustible (> 96 % of world's surface

water) [9,10]. On the other hand, the seawater splitting has been considered as a promising solution for the effective desalinizing saltwater to fresh water, which was characterized with the advantages of low-cost [11,12]. Currently, although Pt and Ru/Ir-based materials are known as state-of-the-art electrocatalyst for overcoming sluggish electrode reactions, its widespread application is impeded by natural scarcity and high cost [13–15]. Consequently, tremendous efforts have been applied in exploring non-precious, low-cost electrocatalysts with high catalytic activity [16]. However, due to the various impurities (Cl$^-$, Ca^{2+}, Mg^{2+}, marine microorganism, particulate matter and so forth) presenting in seawater, several bottlenecks still exist in developing direct seawater electrolysis [10]. Typically, the complex solvent environments could not only lead to precipitations attaching on the cathode (due to the pH drop) but also cause serious chlorine ion corrosion and chlorine

---

evolution reaction (CLER) on anode, which leads to catalyst deactivation and instability. Therefore, there is an urgent need to synthesize robust and effective no-precious catalysts for seawater electrolysis.

Recently, the alloy based on 3d transition metals (such as Fe, Co, Ni) have been investigated as promising electrocatalyst due to the tunable combination and abundant active sites [17–19]. Among them, the Ni-based alloy has been demonstrated to be advanced material, which exhibited appropriate free energy of adsorbed hydrogen intermediate (ΔG_{H^*}) and the satisfactory largest exchange current density according to the volcano plots, thus leading to superior HER activity to other elements (Ni > Co > Fe > W > Cu) [20]. However, it was hard for Ni to separate with hydrogen due to the exceedingly strong affinity, which hindered the HER process [21,22]. Meanwhile, the kinetic and thermodynamic restriction made it difficult for single Ni to achieve satisfactory OER activity. The introduction of Fe could not only induce partial charge transfer of Ni center and promote adsorption/desorption of H_{ad}/OH_{ad}, but also form binary active sites and rich valence states, which gave rise to synergistic effect leading to improved HER and OER processes [23,24]. Therefore, the NiFe alloy was supposed to be prospective bifunctional electrocatalysts due to the intrinsic activity. For example, MoC_2-doped FeNi alloy NPs constructed by Lin's group showed promising bifunctional electroactivity, which achieved the current density of 10 mA cm^{-2} at 1.53 V [25]. Wang *et.al.* fabricated NiFe alloy nanoparticles coupled with N-doped carbon shell via ingenious MOF-annealing process, which only owned the overpotential of 226 mV to achieve 10 mA cm^{-2} for OER [18]. Despite enormous achievements in FeNi-alloy catalysts, the active site was inevitably susceptible to corrosion and agglomeration in harsh environment, especially in seawater, which caused a dramatic decay in activity and mechanical stability [26]. Besides, the inherently low electrical conductivity of alloy is far from satisfactory, which was also an obstruction for enhancement of catalytic activity in seawater splitting and hindered their large-scale application. In this regard, it was of vital importance for NiFe-alloy catalysts to search a straightforward method, which triggered the catalyst performance and stability in seawater. To address these drawbacks, integrating of Molybdenum oxides to form a heterogeneous structure has been widely designed to synthesize high-active electrocatalysts, in which the introduction of molybdenum oxides could not only facilitate interfacial charge polarization leading to optimized bonding with reactive intermediate [27], but also be expected to improve the chemical and mechanical stability of electrocatalysts. For instance, Hu et al. prepared a in situ integrating $MoNi_4$ alloy/MoO_{3-x} heterogeneous structure, which showed outstanding HER activity (17 mV @ 10 mA cm^{-2}) with satisfied long-term stability (over 20 h) [28]. Han et al. designed a micro-nano porous MoO_2 @CoMo HER catalyst, wherein the synergetic effect at the interfaces endowed the catalyst with low overpotential of 76 mV at current density of 50 mA cm^{-2} [29]. In this context, it was available to integrate NiFe alloy with Molybdenum oxides to achieve targeted high catalytic activity.

Conventional methods such as traditional temperature-programmed chemical vapor deposition (CVD) to prepare electrocatalyst was significantly limited by surface oxidation, aggregation, excessive energy and time consumption [30], which lead to the degradation of nanomaterials properties and hamper industrial applications. Hence, it was of vital importance to find effective method to design and synthesize advanced NiFe-alloy electrocatalysts materials with abundant interfaces.

In this work, a NiFe-MoO_2 heterostructure was designed and constructed as an efficient bifunctional electrocatalyst by a novel fast Joule heating technique. The as-prepared FeMoNi/NF integrated the merits of nanorod arrays with large specific surface areas and interface engineering, which exhibited remarkable electrocatalytic activities of HER/OER and was superior to our previous work [31] in alkaline seawater. Meanwhile, during the rapid heating/cooling process, the FeMoNi/NF exhibited face-centered cubic phase for $Fe_{0.5}Ni_{0.5}$ alloy and could further optimize the Fe-Ni bonds, electrical conductivity and achieve more O defects, causing better electrochemical properties than FeMoNi/NF-C

(synthesized by CVD). Additionally, the synergetic interactions at the interfaces of alloy-metal oxides as well as the mechanistic research on catalytic sites towards HER/OER were also revealed by DFT calculations. As expected, the as-prepared FeMoNi/NF displayed outstanding activity in two-electrode configuration and practical MEA electrochemical reactor for overall splitting, which showed feasibility in practical application. Finally, we presented a PV-assisted water electrolysis system with FeMoNi/NF electrodes and home-made polymer solar cells (PSC), which achieved a remarkably STH efficiency of 12.47 %.

2. Experimental section

2.1. Synthesis of NiMoO₄

First, the 4 cm × 3 cm Ni foam (NF) was treated in 2 M HCl solution for 30 min under ultrasonication. Then, the NF was transferred to a breaker containing ethanol solution, which was treated for 30 min under ultrasonication. Finally, 1.0 mmol of $Ni(NO_3)_2 \cdot 6 H_2O$ and 0.4 mmol of $(NH_4)_2Mo_2O_7 \cdot 4 H_2O$ were dispersed in the 75-mL de-ionized (DI) water, which was transferred to a 90-mL Teflon-lined autoclave with as-prepared NF and heated at 150 °C for 6 h to obtain yellow $NiMoO_4$. As-synthesized $NiMoO_4$ on NF was washed with DI water and ethanol for further use.

2.2. Synthesis of FeMoNi/NF

$NiMoO_4$ on NF with a size of 1 cm × 2 cm was soaked in a 0.3 g mL^{-1} $Fe(NO_3)_3$ solution for 15 s and dried under vacuum, which was donated as $Fe-NiMoO_4$. After that, the $Fe-NiMoO_4$ precursor was placed on the center of molybdenum boat which was assembled on the Joule heating equipment (Hefei in situ technology Co., Ltd. China). And then, the chamber of the equipment was vacuumed, which aimed to exclude the influence of air. Finally, the sample was heated for 180 s at the current intensity of 80 A under 200 mL min^{-1} Ar-H_2 (10 %) flow, which was denoted as FeMoNi/NF. The preparation of MoNi/NF catalyst was the same as that of FeMoNi/NF, excepted that the $NiMoO_4$ was directly heated without soaking of $Fe(NO_3)_3$ solution. Similarly, the preparation of FeMo/NF catalyst was the same as that of FeMoNi/NF, except that the $Ni(NO_3)_2 \cdot 6 H_2O$ was removed in the hydrothermal reaction. In the case of Mo/NF catalyst, it was prepared by the same route of FeMo/NF, excepted that the Fe source was not added in the soaking process.

2.3. Synthesis of FeMoNi/NF-C

The $Fe-NiMoO_4$ precursor was placed on the center of porcelain boat which was assembled on the tube furnace. After that, the chamber of the equipment was vacuumed, which aimed to exclude the influence of air. After heating to 900 °C at rate of 5 °C/min under 200 mL min^{-1} Ar-H_2 (10 %) flow, a NF covered with gray-black catalyst was obtained, which donated as FeMoNi/NF-C.

2.4. Materials characterization

To explore the phase structure and surface chemistry of as-prepared catalysts, the X-ray diffraction (XRD) was employed, which was carried out on the Rigaku Miniflex 600 (Cu Kα radiation, scan rate 10° min^{-1}). Meanwhile, the X-ray photoelectron spectroscopy (XPS) was also applied by the Thermo Scientific K-Alpha to insure the chemical states of surface. The structural morphologies of the catalysts were characterized by the transmission electron microscopy (TEM) (JEOL JEM 2100) and scanning electron microscopy (SEM) (Zeiss Gemini 300) which was coupled with Energy Dispersive Spectrometer (EDS). The Raman spectroscopy was recorded on the RENISHAW plc.

2.5. Electrochemical measurements

For the electrochemical measurements, the electrochemical workstation (CHI660E) was applied, which was coupled with three-electrode system in the alkaline seawater (pH 14). Specially, the seawater was collected in the South Yellow Sea (35°55E, 120°42 N), which was further treated by KOH. In the three-electrode system, the Hg/HgO electrode used as reference electrode, while Platinum sheet was used as the counter electrode and the fabricated catalysts were applied as working electrodes for HER/OER tests. For the preparation of 20 wt% Pt/C and RuO_2 electrodes, 10 mg catalyst powder was uniformly dispersed in the 5 mL solution containing the Nafion and ethanol (Nafion: ethanol = 1: 9), which was dropped on the 1 cm × 1.5 cm NF and dried overnight at room temperature. The measured potentials were converted to the RHE by the Nernst equation (E_{RHE} = E_{SCE}+0.098 V + 0.0592 pH). To evaluate the activity of as-prepared samples for HER and OER, the linear sweep voltammetry test (LSV) was carried out with removing the IR drop at a scan rate of 5 mV s^{-1}, which could also be transferred to the Tafel slopes. To calculate the double-layer capacitance values (C_{dl}), the cyclic voltammetry (CV) curves were investigate at a scan rate of 2–10 mV s^{-1}, respectively. The electrochemical impedance spectroscopy (EIS) measurements were performed at open circuit potential, wherein the frequency ranged from 10^{-5} to 10^{-2} Hz. In addition, to investigate the activity of overall splitting, two-electrode configuration was performed. For the stability test of HER, OER and overall splitting, the fabricated systems were conducted under a constant current density without iR drop compensation. To calculate the H_2 turnover frequency (TOF), the current density (j) from LSV and the number of active sites (m) were measured, wherein the m could be obtained in the CV test among PBS solution. The test in MEA was recorded in the YJ-MEA-2020, which could couple with the electrochemical workstation (CHI660E). The generated H_2 and O_2 could be separated by the anion-exchange membrane (FAA-3–50) for further calculation. Subsequently, the power consumption per unit of hydrogen production in MEA could be calculated as following equation: $W = \frac{IUT}{Q_{H_2}*10^3}$, where I, U was assigned to operating current and voltage in the electrolyzer, T was related to the operating time, while Q_{H_2} was the hydrogen generated by MEA.

2.6. Density functional theory (DFT) calculations

The first-principle calculations were carried out by the Vienna *Ab initio* simulation package. For the optimization of the structure, the energy convergence criteria were determined to be 10^{-5} eV and − 0.01 eV/Å, wherein the plane wave basis set cut-off energy was 300 eV. The gradient approximation (GGA) with the Perdew−Burke−Ernzerhof (PBE) parameterization was performed for the exchange-functional [32,33]. In addition, the 3 × 3 × 1 k-point mesh was set for geometry optimization.

2.7. Fabrication of solar-driven electrolysis system

The J–V characteristics of the polymer solar cell were tested by the KEITHLET 2400, wherein the solar-derived water splitting device was measured by the CHI660. The simulated sunlight was performed by the 300-W xenon lamp with AM 1.5 G optical filter (100 mW cm^{-2}). For the verification of practicality, the outdoor test was performed in Qingdao, China (120°49′E, 36°16′N), at 10:00 a.m. BST, wherein commercial silicon cell was connected to the FeMoNi/NF // FeMoNi/NF electrolyzer.

The polymer solar cell was prepared in the glovebox, wherein the temperature (25 °C), water (0.1 ppm) and oxygen (0.1 ppm) could be maintained. The additive was obtained by dispersing a mixture of D18, Y6 and BTP-eC9 active layers in chloroform containing 0.5 vol% of 1,8-diiodooctane (DIO). Indium tin oxide (ITO) glass was taken as the substrate, where the structure of the fabricated device was ITO/PEDOT: PSS/active layer/DINO/Al. After the sonication of ITO in detergent solution, acetone and isopropanol, respectively, UV-ozone was applied. The PEDOT:PSS (CLEVIOS PVP AI 4083) film (40 nm) was spin-coated onto treated ITO substrates at 4500 rpm for 20 s, which was thermally annealed at 150 °C for 10 min. The active layer was deposited on the PEDOT:PSS layer, which was annealed 100 °C for 15 min. Finally, the layer of PDINO in Methanol was formed on the such active layer via spin-coating. The Al was deposited after the thermal evaporation under 4×10^{-4} Pa. To reach enough photo-voltage, two single polymer solar cells were linked together in series, which was integrated with the FeMoNi/NF // FeMoNi/NF electrolyzer. The STH efficiency of system was calculated by the equation: STH(%) = 1.23(V) × I(mA cm^{-2}) × 100/$P_{simulated\ solar}$, wherein the $P_{simulated\ solar}$ was the energy for simulated solar, while the I was the current density measured in the solar-derived water splitting device.

3. Results and discussion

3.1. Synthesis and material characterizations

The final porous and self-supported FeMoNi/NF sample with NiFe alloy/MoO_2 heterostructure was successfully fabricated by simple three-step process of hydrothermal method, soaking and rapid Joule heating, as shown in Fig. 1a. First, the hydrothermal method was applied to fabricated the $NiMoO_4$, wherein the pre-treated Ni foam was chosen as three-dimensional substrate. Then, as-prepared $NiMoO_4$ template was soaked in the $Fe(NO_3)_3$ solution at room temperature to form the Fe-$NiMoO_4$. Finally, the black FeMoNi/NF catalyst was obtained by annealing under H_2/Ar atmosphere via rapid Joule heating. Typically, the detailed Joule heating setup was shown in Fig. S1.

The structural information of the as-prepared catalysts was measured by the XRD. Fig. S2 confirmed that the phase of $NiMoO_4$ precursor was the mixture of the $NiMoO_4$ (PDF # 12-0348) and $NiMoO_4 \cdot xH_2O$ (PDF # 13-0128). After soaking with $Fe(NO_3)_3$ solution, there was no apparent shift of the diffraction peak, which proved that $Fe(NO_3)_3$ etching only occurred at the surface level [34]. Following calcination via Joule heating, the diffraction peaks at 2θ = 26.3°, 37.3°, 53.9°, 60.8° and 79.2° could be attributed to the MoO_2 phase (PDF # 97-002-3722), wherein the 43.8°, 51.1° and 75.3° could be indexed to the NiFe alloy phase (PDF # 04-006-6384) as shown in the Fig. 1b, verified that the introduced Fe atoms could integrate with Ni atoms to synthesize NiFe alloy. Interestingly, it should be noted that the introduction of Fe species facilitated the formation of NiFe alloy while the content of MoO_2 was reduced, as compared to the diffraction peaks of MoNi/NF in Fig. 1b. Such phenomenon might be interpreted by the sequential reduction which occurred in the pyrolysis process among the reductive atmosphere [35]. Typically, the reductive reaction of Fe and Ni species preferentially occurred in Fe-$NiMoO_4$ precursor, which could be demonstrated by the relevant standard molar enthalpies of formation (ΔH^{Θ}) at 298 K as shown in Fig. S3. Specifically, the ΔH^{Θ} (298 K) of NiO and Fe_2O_3 was − 239.8 kJ mol^{-1} and − 824.3 kJ mol^{-1}, respectively, which were much lower than $MoO_3 \cdot H_2O$ (−1037.3 kJ mol^{-1}) and $MoO_3 \cdot 2\ H_2O$ (−1335.0 kJ mol^{-1}) [36].

To investigate the morphology transformation of these materials during synthesis process, the SEM images was applied. As shown in Fig. S4, the initial NF exhibited smooth surface. After the hydrothermal process, nanorods-shaped $NiMoO_4$ precursor were grown on the NF, which aggregated to form nanosphere with the diameter in the range of 50–70 μm (Fig. S5). Followed by $Fe(NO_3)_3$ solution soaking, the formed Fe-$NiMoO_4$ remained the highly-dispersed nanorods morphology (Fig. S6) and the surface (Fig. 1c) became rougher compared to $NiMoO_4$ (Fig. 1d), which might be caused by the $Fe(NO_3)_3$ etching. Furthermore, the elements distribution and approximate stoichiometry for the elements Mo, O, Fe and Ni in the Fe-$NiMoO_4$ were investigated by the corresponding energy dispersive spectroscopy (EDS), wherein the
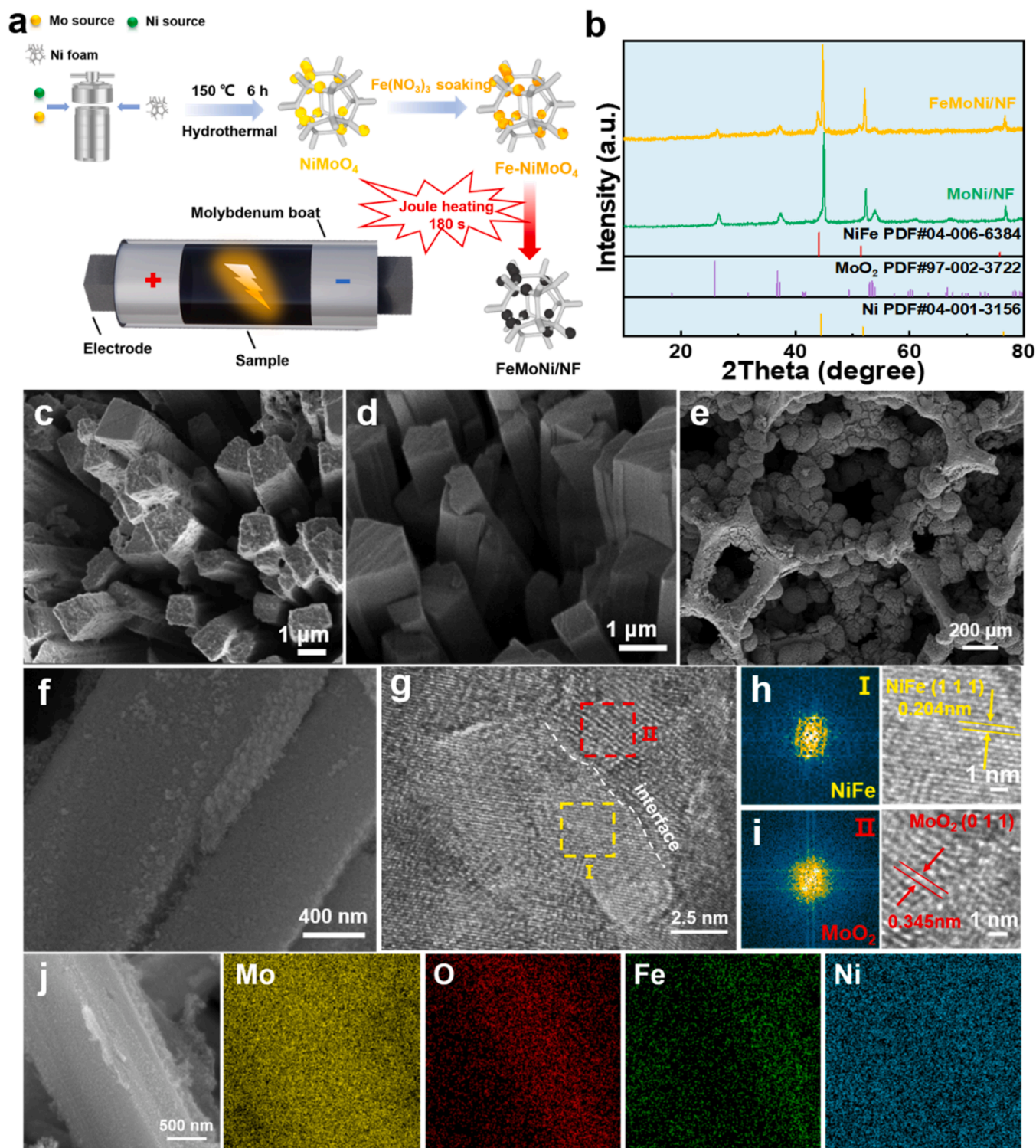
Fig. 1. (a) Schematic illustration of the synthesis process for self-supported FeMoNi/NF, (b) XRD patterns of FeMoNi/NF and MoNi/NF, (c, d) SEM images of Fe-NiMoO$_4$ and NiMoO$_4$, (e, f) SEM images of FeMoNi/NF, (g-i) TEM images of FeMoNi/NF, (j) Elemental mapping of FeMoNi/NF.

elements showed highly uniform distribution (Fig. S7) and the atomic ratio of Mo:O:Ni:Fe $\approx$ 12.7:9.6:9.9:1 was confirmed (Fig. S8). After Joule heating, the morphology-preserved FeMoNi/NF nanorods fully overlaid the entire NF, which also collectively formed the nanosphere as shown in the Fig. 1e. Meanwhile, the rough surface was formed due to high-temperature calcination(Fig. 1j), and the low interfacial adhesion energy may be favorable to the adsorption of electrolytes and desorption of hydrogen bubbles [37]. The excellent maintenance of nanorods might

be accredited to the heterogeneous composition of the microscale [38], which could be proved by the TEM image (Fig. 1g). The typical inter-planar spacings of 0.204 and 0.345 nm (Fig. S9) were well-indexed to the (1 1 1) plane of NiFe alloy (Fig. 1h) and the (0 1 1) plane of MoO$_2$(Fig. 1i) [27], respectively, wherein the visible interface coupled with XRD results indicated the successful synthesis of heterostructure. For further demonstration, the SEM of MoO$_2$ (Fig. S10a) and FeMoNi/NF (Fig. S10b) with high magnification were applied, wherein NiFe alloy

with nanoparticle structure was covered on the nanorods surface for the MoO_2 confirming the synthesis of NiFe alloy/MoO_2 composites. Moreover, the EDX point scanning were conducted to measure the composition and distribution of elements in nanoparticles (Fig. S11). Compared with the MoO_2, the content of element Fe among nanoparticles was increased from 4.95 % to 12.47 %. On the other hand, the HRTEM of FeMoNi/NF also presented that the nanoparticles were consisted of NiFe alloy, which could be correlated to the fringe spacings of 0.200 nm (1 1 1) and anchored on the MoO_2 nanorod (Fig. S12). With the aforementioned statements, the successful synthesized NiFe alloy/MoO_2 heterostructure was confirmed. The construction of heterogeneous interfaces played an important role in tailoring the electronic structure and refining intermediate binding capability, which was beneficial to the intrinsic activity of catalysts [39]. Moreover, the EDS spectrum illustrated uniform distribution of Fe, Mo, Ni and O elements on nanorod (Fig. 1j) with the ratio of 1:10.3:8.6:2.3 (Fig. S13).

The variation for surface chemical compositions and electronic interactions has been considered as a critical factor for improving the activity of the catalyst. And the XPS was conducted to reveal the surface compositions of FeMoNi/NF, wherein the sample without Fe species (MoNi/NF) was also measured for comparison. For the high-resolution XPS orbital scan of Ni 2p of FeMoNi/NF (Fig. 2a), two valence states can be detected: Ni^0 $2p_{3/2}$ and Ni^0 $2p_{1/2}$ at 852.7 eV and 870.1 eV, Ni^{2+} $2p_{3/2}$ and Ni^{2+} $2p_{1/2}$ at 856.2 eV and 874.0 eV, which could match with

the metallic nickel and surface oxidation, respectively. The additional peaks at 862.1 eV and 880.2 eV were assigned to satellite peaks (donated as Sat.). It should be noted that the Ni 2p peaks of FeMoNi/NF slightly shifted to low binding energy relative to MoNi/NF, proving electron transfer to Ni due to the presence of Fe, which could modulate the ionophilicity of Ni thus leading to enhanced activity for OER process [40,41]. In Fig. 2b, the Mo 3d XPS of FeMoNi/NF showed four valence states of Mo^{6+} (232.3 eV and 235.5 eV), Mo^{5+} (230.5 eV and 233.8 eV), Mo^{4+} (229.3 eV and 232.6 eV) and Mo^0 (228.4 eV and 231.5 eV), wherein the relatively low valence states of Mo^{5+}, Mo^{4+} and Mo^0 indicated the reduction from Fe-$NiMoO_4$ precursor due to reductive atmosphere [42]. Compared with MoNi/NF, the apparent positive shift for Mo 3d in FeMoNi/NF showed intense electronic interactions among NiFe alloy/MoO_2 heterostructure. To better emphasize the role of Joule heating under H_2/Ar atmosphere, the XPS spectra of $NiMoO_4$ precursor was also measured. As shown in the Fig. S14a and S14b, no characteristic peaks of metallic nickel in Ni 2p and metallic molybdenum with other relatively low valence states in Mo 3d could be found, further demonstrating the reductive evolution of molybdate. As depicted in Fig. 2c, the main peaks were located at 710.5 eV and 723.0 eV, which was ascribed to the Fe^{3+}, while other peaks at 705.8 eV and 716.1 eV originated from the Fe^0. Consequently, the above obvious signals of Fe^0 and Ni^0 further confirmed the presence of NiFe alloy, which was consistent with the XRD result. Additionally, in comparison to MoNi/NF,
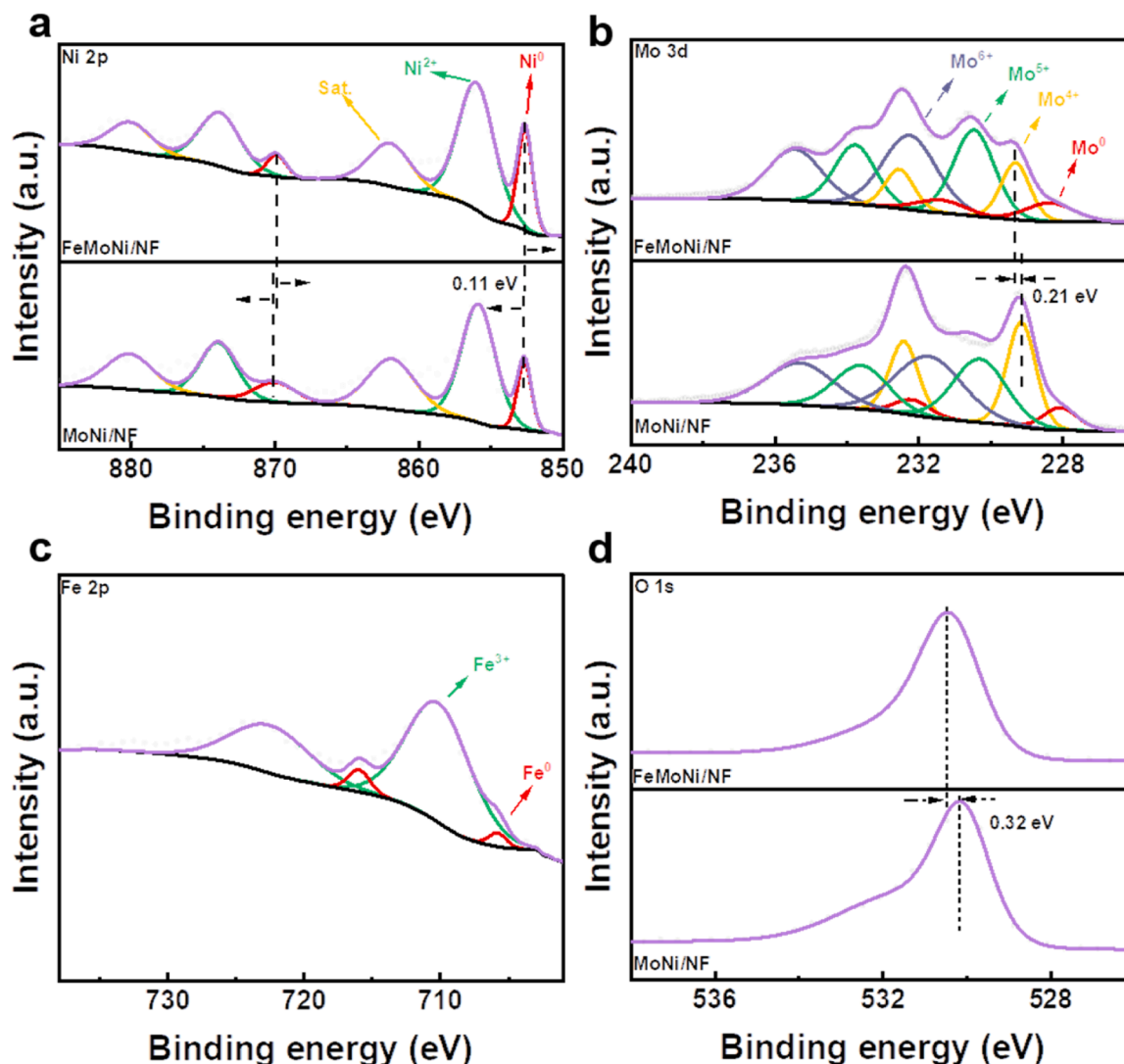

Fig. 2. XPS spectra of FeMoNi/NF and MoNi/NF: (a) Ni 2p; (b) Mo 3d; (c) Fe 2p and (d) O 1 s.

the binding energy of O 1 s in FeMoNi/NF were shifted positively 0.32 eV, indicating an electron redistribution after coupling NiFe alloy with MoO_2, which was conducive to moderating the adsorption/dissociation energies of intermediates [34].

3.2. Electrocatalytic performance for HER

The HER performance of the FeMoNi/NF and other obtained catalysts were analyzed by three-electrode system under 1.0 M alkaline seawater with iR-correction, wherein the measured potentials were transferred to reversible hydrogen electrode (RHE). For comparison, MoNi@NF, FeMo@NF, Mo@NF, NF and benchmark Pt/C catalyst were
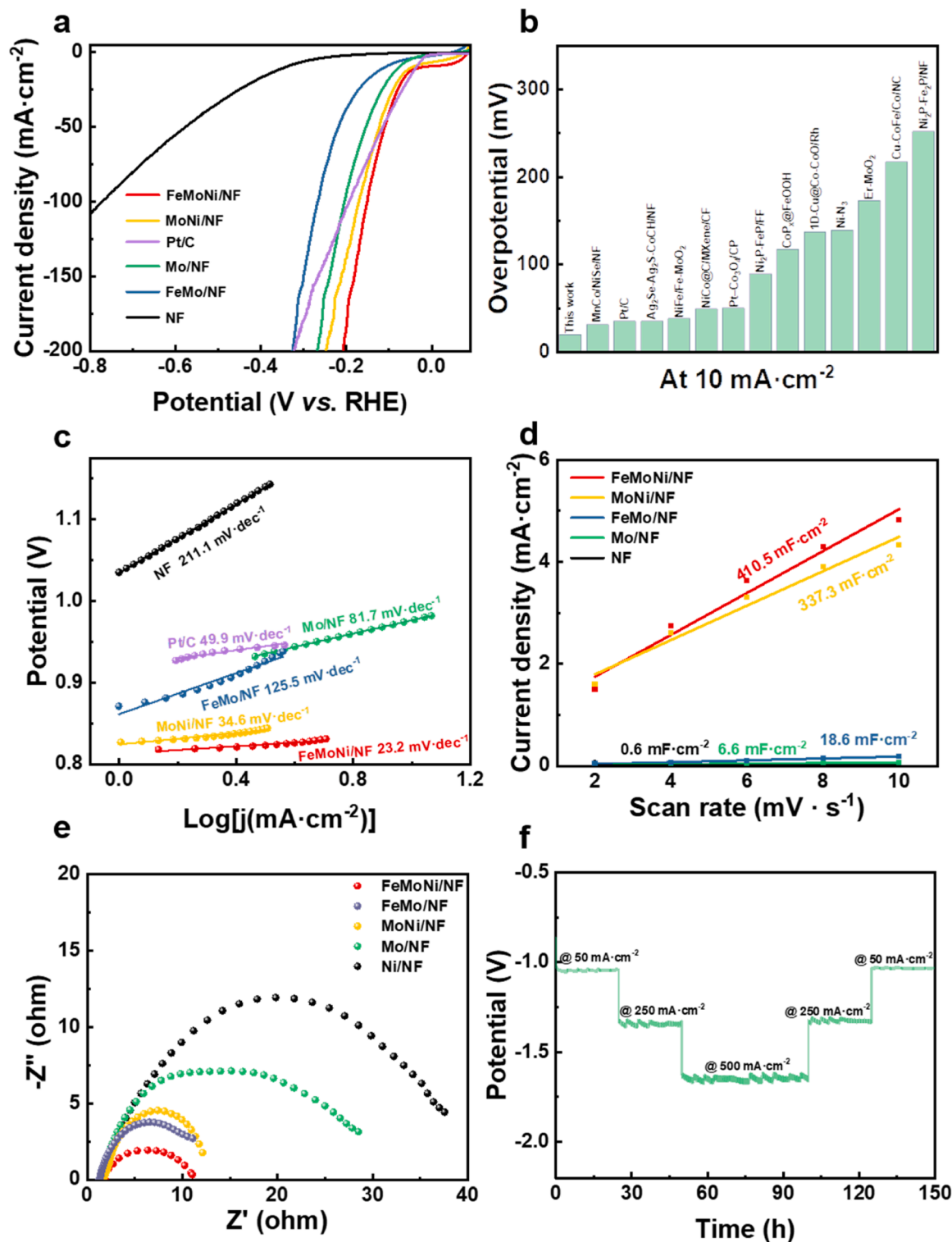

Fig. 3. (a) LSV curves of various catalysts, (b) Comparison of HER performance of FeMoNi/NF with other electrocatalysts ($j = 10$ mA cm^{-2}) tested in alkaline seawater, (c) Tafel plots, (d) C_{dl} and (e) EIS plots of various catalysts. (f) Chronopotentiometry at 50, 250 and 500 mA cm^{-2} of FeMoNi/NF in alkaline seawater electrolyte.

also explored under the same condition with FeMoNi/NF. According to the LSV curves in Fig. 3a, as-prepared FeMoNi/NF exhibited outstanding HER activity with the low overpotential of 20 mV at 10 mA cm^{-2}, which was even lower than that of state-of-art Pt/C electrode (36 mV at 10 mA cm^{-2}) and other samples. Such activity might be due to the unique heterostructure of metal and metal oxide in FeMoNi/NF, which effectively optimize the electronic structure and accelerate electron transfer, thus lowering the reaction barrier for HER process. Furthermore, such excellent activity also outperformed recently reported HER electrocatalysts in alkaline seawater as shown in Fig. 3b, wherein the detailed overpotentials were reflected in Table S1. To further explore HER performances, the relevant Tafel slopes were investigated, which were driven from the LSV curves and correlated with the catalyst kinetics. The calculated value (Fig. 3c) showed the lowest slope (23.2 mV dec^{-1}) of target FeMoNi/NF, much smaller than that of other catalysts, revealing the rapid reaction kinetics. Meanwhile, such Tafel slope of FeMoNi/NF reflected a conventional Volmer-Tafel mechanism, in which the rate-determining step (RDS) was associated with the H$_2$ desorption (Tafel step) [43,44]. In order to further explore the mechanism of enhanced activity in FeMoNi/NF, the value of double-layer capacitances (C$_{dl}$) was obtained via the CV curves in non-Faradaic region (Fig. S15), which was positively correlated with electrochemical surface area (ECSA). As shown in Fig. 3d, the values of C$_{dl}$ were calculated to be 410.5, 337.3, 18.6, 6.6 and 0.6 mF cm^{-2} for FeMoNi/NF, MoNi/NF, FeMo/NF, Mo/NF and NF, respectively, meaning more exposed electrocatalytic active sites among FeMoNi/NF. Such result might be ascribed to the rough surface and Fe incorporation, which played an important role in enhancing the HER activity. For activity normalization, the turnover frequency (TOF) values of the FeMoNi/NF, MoNi/NF, Mo/NF and FeMo/NF were measured via electrochemical method (Fig. S16a), which provided an indication of the intrinsic catalytic activity by presenting the number of hydrogen molecules formed per second at each active site [45,46]. Table S2 exhibited the calculated number of active sites of mentioned samples. For FeMoNi/NF, the TOF value reached 4.1 s^{-1} at the overpotential of 100 mV (Fig. S16b), which was much higher than MoNi/NF (3.3 s^{-1}), Mo/NF (1.3 s^{-1}) and FeMo/NF (1.2 s^{-1}), indicating the superiority of the HER intrinsic activity. In addition, EIS, as a crucial parameter for catalytic kinetics, were also probed. It was found that FeMoNi/NF possessed the smallest semicircle diameter (Fig. 3e) and the smallest charge transfer resistance (Rct) of 9.7 Ω, which was calculated from fitted circuit diagram (Fig. S17) demonstrating the most rapid interfacial charge transfer kinetics and the best electronic conductivity based on the Nyquist plots.

Apart from the catalytic activity, the durability of FeMoNi/NF was further tested (Fig. 3f), which manifested the commercial application in alkaline seawater at the constant high current density of 50, 250 and 500 mA cm^{-2}. During the long-term chronopotentiometry test, the measured *v-t* curve displayed little attenuation within 150 h, verifying superb durability and chlorine corrosion resistance for FeMoNi/NF, which might be caused by the in-situ formed NiFe alloy/MoO$_2$ heterostructure structure [39]. Besides, Raman spectra of FeMoNi/NF before and after the HER process displayed identical peaks (Fig. S18), implying outstanding electrochemical durability. After whole HER process, the morphology of FeMoNi/NF still showed nanorods except appeared cross-linking together (Fig. S19), which confirmed distinguished stability for FeMoNi/NF in alkaline seawater. The XPS spectra before and after the HER process were obtained, wherein the Ni^{2+} state dominantly existed and Ni^0 state decreased after long-term chronopotentiometry (Fig. S20). Furthermore, the Mo^{4+} in MoO$_2$ was more oxidized to Mo^{6+} and most of Fe existed in Fe^{3+}, which meant the FeMoNi/NF electrocatalysts was evolved to Fe/NiOx@MoO$_6$. For verification, the XRD pattern of FeMoNi/NF was measured after 150 h chronopotentiometry, wherein the NiFe phase was almost disappeared and the phase of MoO$_2$ dissolved to some extent, as shown in Fig. S21. The above results demonstrated that the FeMoNi/NF catalyst was characterized with superior HER performance in alkaline seawater.

3.3. Electrocatalytic performance for OER

We then investigated the OER performance of FeMoNi/NF in alkaline seawater under the standard three-electrode system. As shown in the Fig. 4a, the LSV of various catalysts for OER were collected and plotted. Unexpectedly, the FeMoNi/NF owned the lowest overpotential (250 mV) to drive the current density of 50 mA cm^{-2}, much lower than that of commercial RuO$_2$ (410 mV). Additionally, such outstanding OER activity was in competition with the recently reported OER electrocatalysts and our reported catalyst (MoNi/NF) that were applied among the alkaline seawater (Fig. 4b and Table S3 and S4) [31]. Additionally, the Tafel value of FeMoNi/NF (Fig. 4c) was as low as 144.9 mV dec^{-1}, which was lower than those of FeMo/NF (159.9 mV dec^{-1}), Mo/NF (192.0 mV dec^{-1}), MoNi/NF (233.9 mV dec^{-1}), RuO$_2$ (275.4 mV dec^{-1}) and NF (294.3 mV dec^{-1}). Besides, the C$_{dl}$ value calculated from CV curves (Fig. S22) of FeMoNi/NF was determined to be 11.6 mF cm^{-2} for OER larger than that of other catalysts (Fig. 4d), suggesting the largest electrochemical capacitance and the most abundant active sites. Meanwhile, the TOF values revealed that FeMoNi/NF owned the most active intrinsic activity among contrast samples (Fig. S23). For FeMoNi/NF, it owned the highest TOF value (10.0 s^{-1}) at the overpotential of 300 mV, much higher than FeMo/NF (5.4 s^{-1}), Mo/NF (1.0 s^{-1}) and MoNi/NF (2.5 s^{-1}). Consistent with the case of HER, the catalyst possessed the smallest semicircle diameter and the smallest charge transfer resistance (Rct) of 0.3 Ω, signifying the superior charge transfer rate, as shown in the Fig. 4e. In addition, the measured *v-t* curve remained unchanged at constant current density of 50, 250 and 500 mA cm^{-2} after 150 h stability test (Fig. 4f), which was evident that FeMoNi/NF owned superior electrochemical stability for OER process. The SEM image in Fig. S24 revealed that the FeMoNi/NF maintained pristine nanorod morphology after long-term OER testing, indicating satisfactory catalytic durability.

It should be emphasized that the measured polarization curve for OER was significantly changed as the number of measurements increased (Fig. S25), implying a variation of the chemical composition, which might be caused by electrochemical reconstruction with the presence of oxidation voltage [16]. In order to investigate the real catalytic active sites for the outstanding OER performance, the LSV curves between 1.2 V and 1.5 V were carried out, as shown in the Fig. 5a. Typically, an obvious anodic peak located at 1.44 V (vs. RHE) of FeMoNi/NF could be observed, which was attributed to Ni^{2+}/Ni^{3+} transition, demonstrating the in-situ formation of FeNi-oxyhydroxide [47]. Compared with the Fe-free MoNi/NF (1.34 V), the positively shifted anodic peak might be caused by the Fe incorporation as shown in Fig. 5a [48]. It could be indicated that the formed oxyhydroxides during the OER process played an important role in active species [46,49]. Furthermore, such result was confirmed by the Raman spectra of FeMoNi/NF before and after OER process (Fig. 5b). The peaks of unreacted catalyst, which was located at 353, 564, 734 cm^{-1}, were from the MoO$_2$. And the peak at 803 cm^{-1} could be assigned to the Mo-O vibration from MoO$_4^{2-}$ [50,51]. After the OER process, two characteristic peaks generated at 469 and 585 cm^{-1} were likely associated to the Ni-O bending vibration and stretching vibration in NiOOH [52], respectively. Moreover, two new bands located at 542 cm^{-1} (Fe-OH asym. str) and 688 cm^{-1} (Fe-O sym. str), may be attributed to FeOOH [53,54]. It has been confirmed that such in-situ formed FeNi-oxyhydroxide was beneficial for highly-efficient OER performance due to the optimal adsorption energy of intermediates [16,52], which led to significant improvement for the OER activity of FeMoNi/NF. Interestingly, it was also found that after OER reaction, the Raman bands of MoO$_2$ was disappeared, while the peak intensity of MoO$_4^{2-}$ was enhanced, indicating the occurrence of oxidation process. Typically, there was a promoting effect for MoO$_4^{2-}$ to optimize the adsorption between OOH* intermediate and active sites, thus leading to enhanced OER activity [55]. In addition, the generated Mo^{6+} was considered to accelerate the formation of FeNi-oxyhydroxide due to the significant
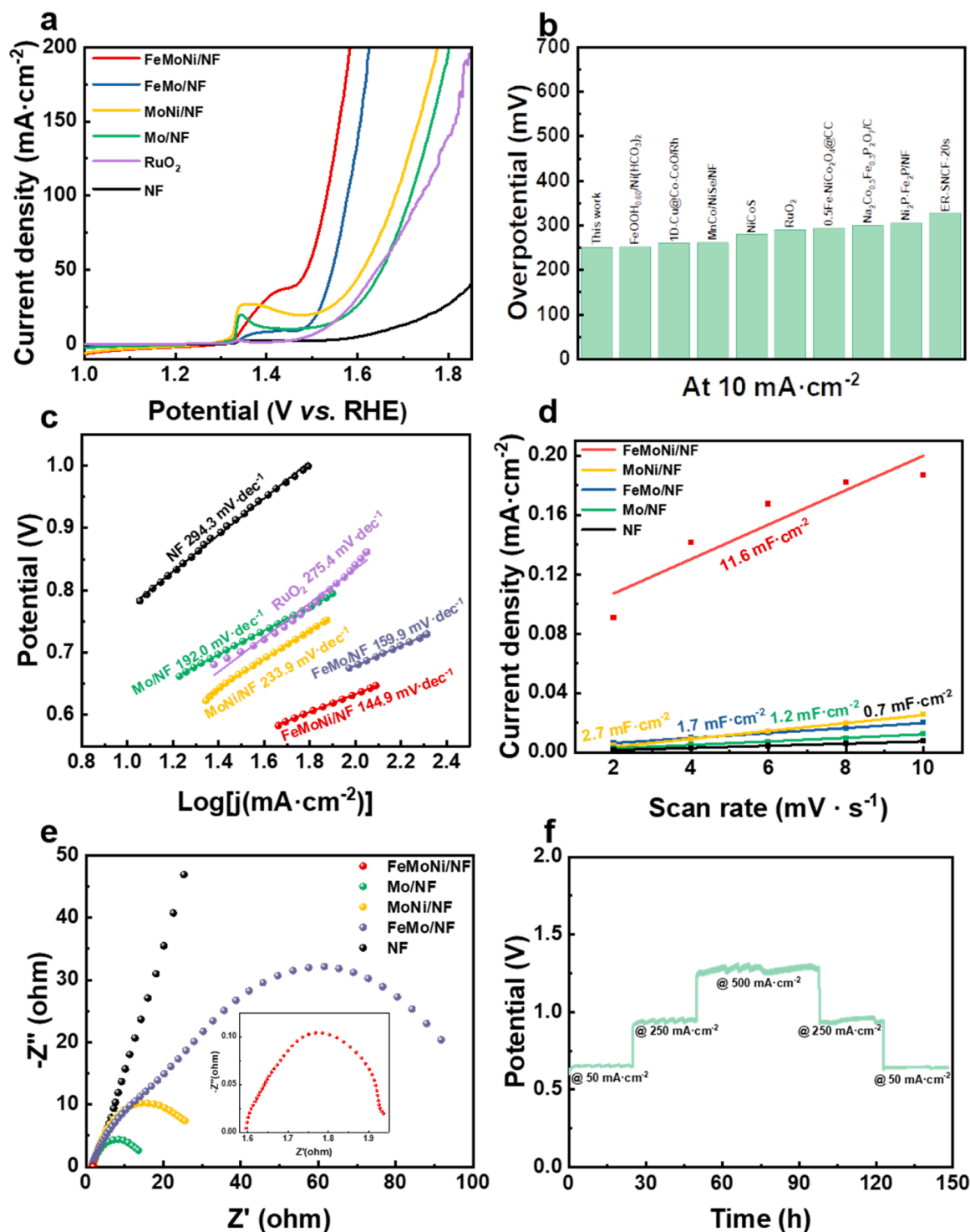
Fig. 4. (a) LSV curves of various catalysts, (b) Comparison of OER performance of FeMoNi/NF (j = 50 mA cm^{-2}) with other electrocatalysts (j = 10 mA cm^{-2}) tested in alkaline seawater (c)Tafel plots, (d) C_{dl} and (e) EIS plots of various catalysts. (f) Chronopotentiometry at 50, 250 and 500 mA cm^{-2} of FeMoNi/NF in alkaline seawater electrolyte.

ability to draw electrons [52].

The FeMoNi/NF before and after OER testing was further revealed with XRD patterns, as shown in the Fig. 5c. The catalyst showed typical characteristic peaks of MoO_2 with the disappeared NiFe alloy peaks, which confirmed that the reconstruction occurred and was identical to the Raman results. For the high-resolution XPS of Mo 3d, Ni 2p and Fe 2p, these three peaks assigned to metallic Mo, Ni, Fe at 228.4 eV, 852.7 eV and 706.5 eV disappeared after OER testing due to the surface

oxidation. On the other hand, the peaks of Mo^{6+}, Ni^{2+}, Fe^{3+} were totally shifted to higher binding energy compared with unreacted catalyst, indicating the formation of metal oxyhydroxides. Consequently, by the results mentioned above, we inferred that in-situ formed (Ni, Fe)OOH during the whole OER process acted as the real active sites [16,56,57].

From the above, the electrochemical reconstruction could be spontaneously occurred on the NiFe alloy, in which the generated active FeNi-oxyhydroxide played a critical role in OER with the remarkable
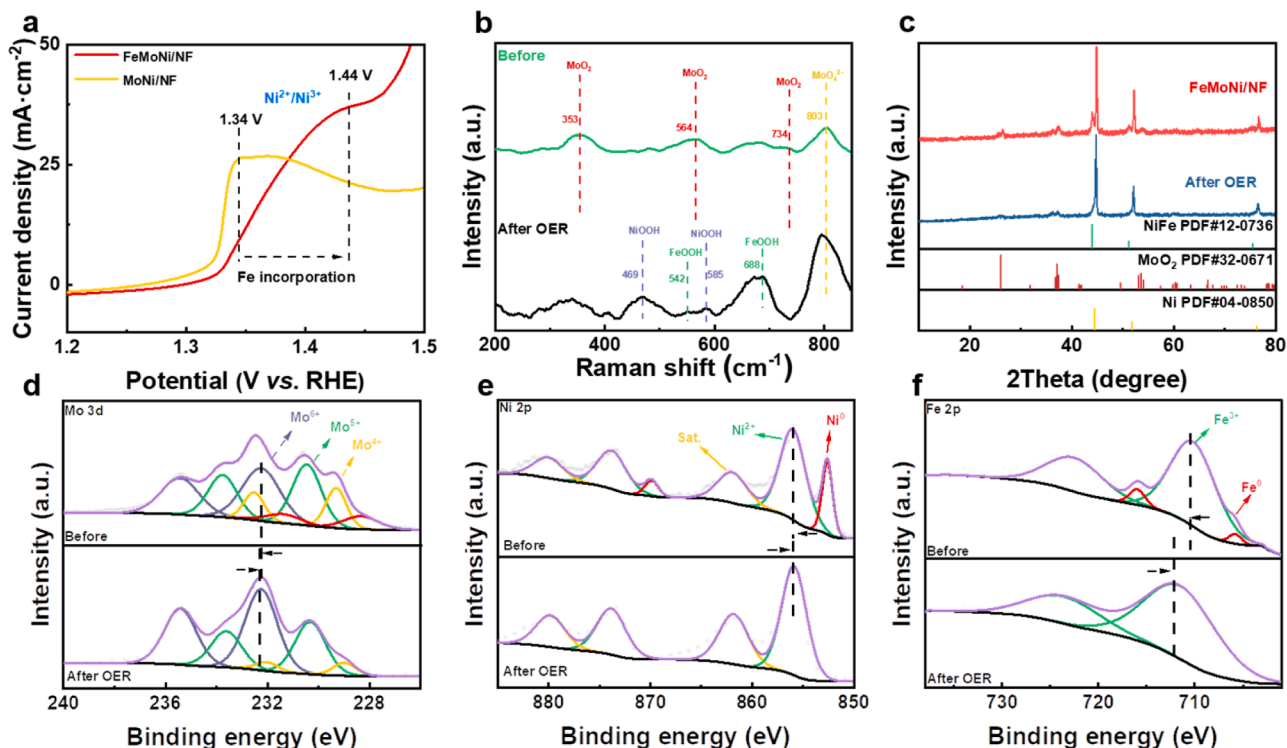
Fig. 5. (a) LSV curves of FeMoNi/NF and MoNi/NF, (b) Raman spectra of FeMoNi/NF before and after OER testing, (c) XRD patterns of FeMoNi/NF before and after OER testing, XPS spectra of FeMoNi/NF before and after OER testing: (d) Mo 3d, (e) Ni 2p and (f) Fe 2p.

ability to optimize the adsorption with intermediate [16]. Therefore, the mechanism of FeMoNi/NF for HER/OER could be postulated as follows: For HER process, the synergy of FeMoNi/NF was well modulated via synergetic interactions at the interfaces of alloy-metal oxides. For OER process, the alloy could be in-situ transferred to oxyhydroxide, which worked as active center. Furthermore, the MoO$_2$ maintained chemical and mechanical stability during the reaction, and accelerated the transfer of electrons for reaction paths of HER/OER (Fig. 6). As a result, such designed FeMoNi/NF not only maintained superior HER performance, but also could be converted and exhibit excellent OER performance, wherein the in-situ transformation of actual active site demonstrated great flexibility for overall water splitting.

3.4. The role of Joule heating

To further emphasize the advance of Joule heating compared with the traditional CVD heating method, heating rate plots were performed in the Fig. 7a and b. Typically, the Joule heating was characterized as fast heating/cooling rate (24 °C/s and 40 °C/s), which provided sufficient condition for the formation of defect, as shown in Fig. S26. It has been widely reported that the in-situ created defect played an important role in modulating the surface electronic structure of electrocatalysts, thus leading to optimized adsorption free energy with intermediate species [58]. On the other hand, such short heating time was conducive to achieve energy efficiency and realize the lower production costs, which manufactured the catalyst with minimal energy waste. As shown in the inset table of Fig. 7a, the rapid Joule heating, as local heating
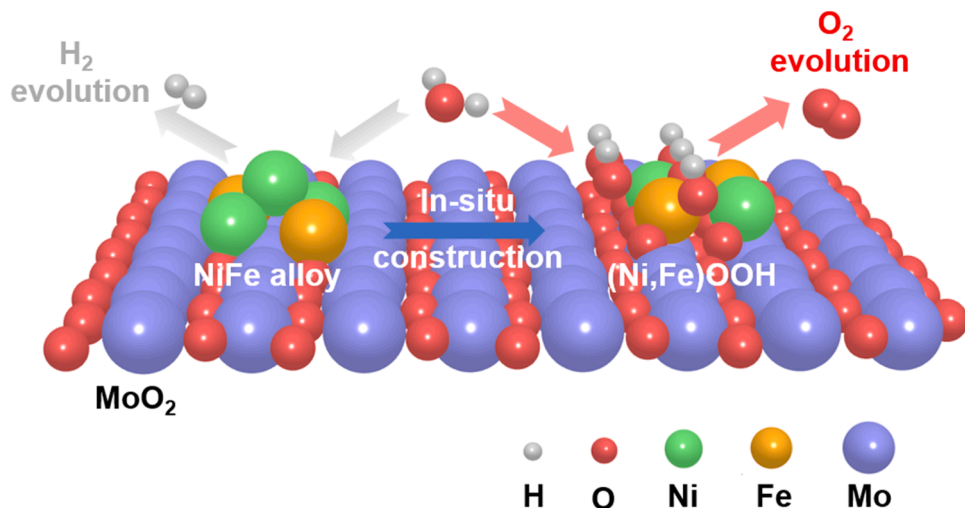

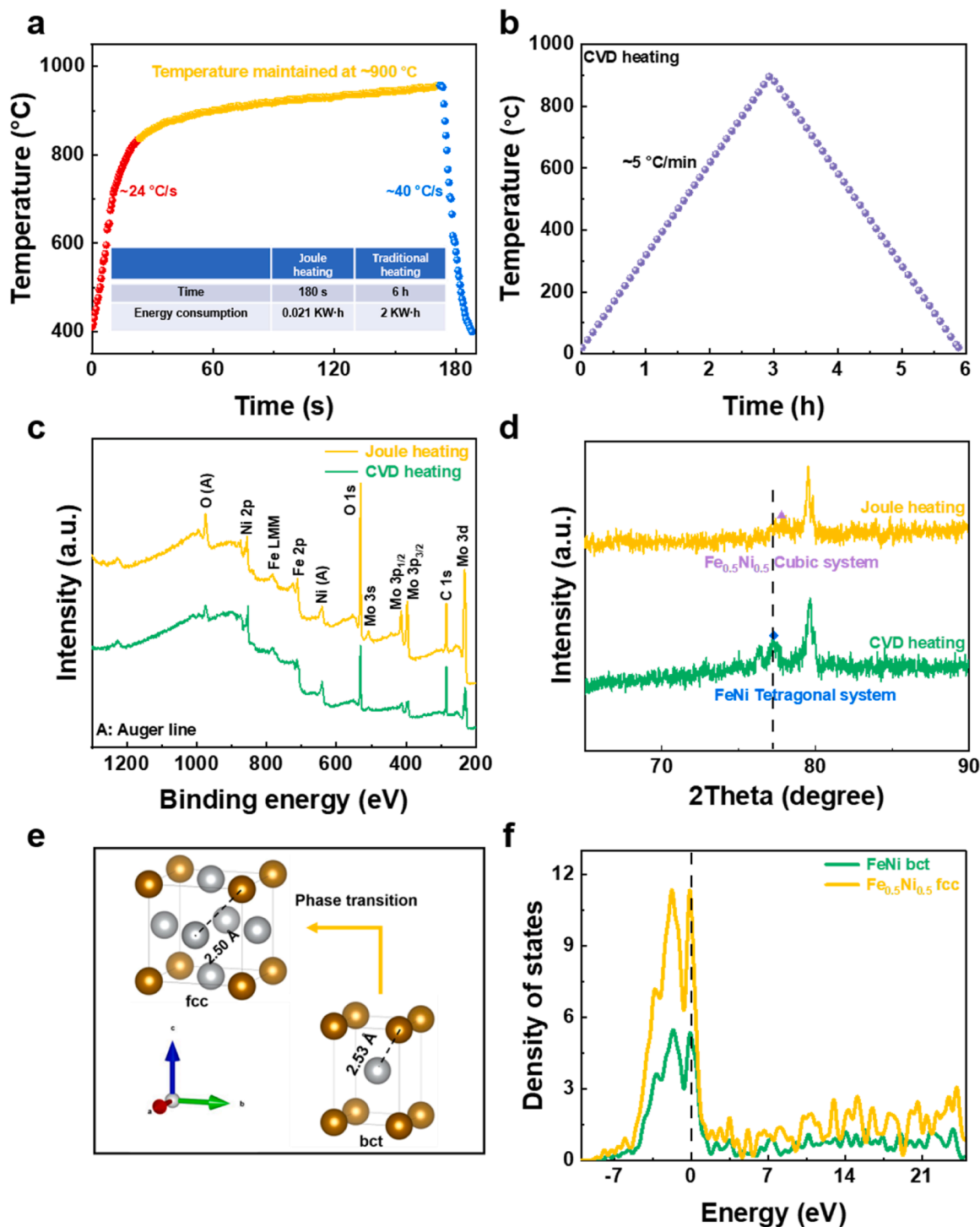**Fig. 6.** Schematic illustration of in-situ construction and HER/OER for catalyst.

Fig. 7. (a) The heating curves of Joule heating and (b) CVD heating method, wherein the inset table exhibited the heating time and energy consumption (calculated by equipment power multiplied by operation time), (c) XPS survey spectra and (d) XRD pattern of FeMoNi/NF and FeMoNi/NF-C, (e) Crystal structure and (f) calculated partial density of states (DOS) diagram of FeNi alloy for fcc and bct.

method, led to not only efficient heating process but also much lower energy consumption than CVD method, which consumed 1.05 % energy of CVD method. In addition, the XPS survey spectra and XRD pattern of FeMoNi/NF and catalyst prepared by CVD method (denoted as FeMoNi/NF-C) were carried out (Fig. 7c and d), which confirmed the same elemental composition (Ni, Mo, Fe, O) and similar phase composition. However, the XRD patterns of FeMoNi/NF and FeMoNi/NF-C were consistent with the face-centered cubic phase $Fe_{0.5}Ni_{0.5}$ (JCPDS# 04-006-6384) and body-centered tetragonal lattice FeNi (JCPDS#

04-008-8265), respectively, wherein the crystal structure could be regulated by the different heating conditions. Notably, the stacking pattern of metal atoms in different crystalline phases yields different electronic properties, which significantly affects the intrinsic catalytic properties of metal alloy nanomaterials [59]. Notably, the length of Ni-Fe bonding for fcc-$Fe_{0.5}Ni_{0.5}$ alloy (2.50 Å) was shorter than bct-FeNi alloy (2.53 Å), which effectively turned the electronic structure for alloy and enhanced the conductivity of catalysts (Fig. 7e). The subsequent DFT result confirmed that the fcc-$Fe_{0.5}Ni_{0.5}$ alloy synthesized by Joule

heating was characterized with electrical conductivity and better metallic behavior than bct-FeNi alloy (Fig. 7f), indicating the advance for rapid heating/cooling process of Joule heating. For comparison, the XPS spectra of FeMoNi/NF and FeMoNi/NF-C were performed for the in-depth exploration of chemical interactions. As shown in the Fig. S27, the Ni, Fe, Mo elements on the surface of FeMoNi/NF and FeMoNi/NF-C were in the form of metal monomers as well as higher valence elements, indicating the similar element composition. However, for the FeMoNi/NF-C, the ratio of Ni^0/Ni^{2+} (0.81:1), Fe^0/Fe^{3+} (0.41:1) and

Mo^0/Mo^{6+} (0.70:1) were much higher than FeMoNi/NF (Ni^0/Ni^{2+} = 0.26:1; Fe^0/Fe^{3+} = 0.20:1; Mo^0/Mo^{6+}= 0.22:1), which might be caused by the prolonged excessive pyrolysis. Meanwhile, there were obvious peaks of surface absorption specie (H-O), lattice oxygen (M-O) and oxygen vacancy (O defect) in the O 1 s spectra of FeMoNi/NF and FeMoNi/NF-C, as shown in Fig. S27d. Notably, the ratio of oxygen vacancy and lattice oxygen in FeMoNi/NF (2.52:1) was much higher than FeMoNi/NF-C (0.68:1), wherein the coordination environment caused by O vacancy gave rise to the electronic structure, thus leading to
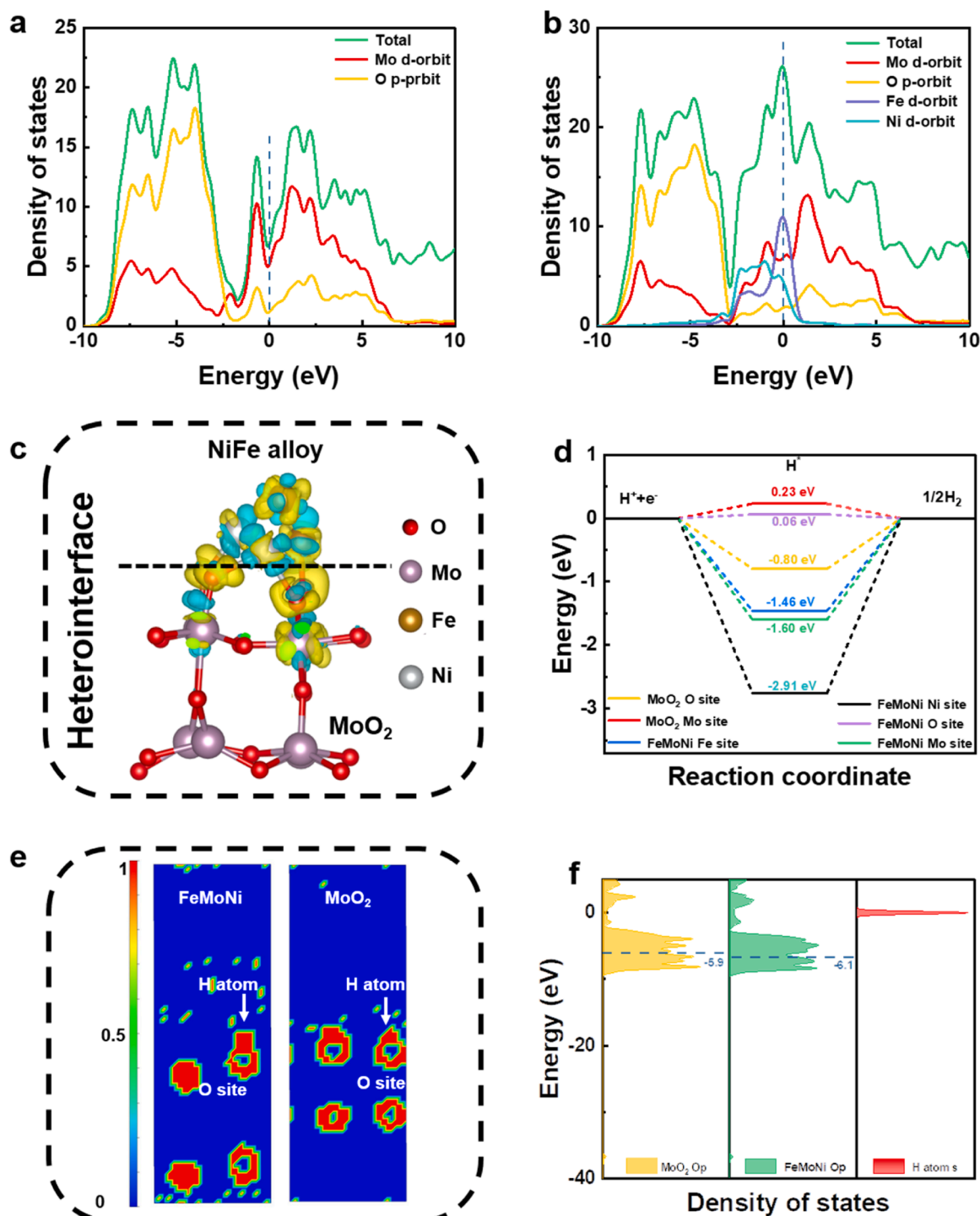

Fig. 8. The calculated partial density of states (DOS) diagram of (a) MoO_2 model and (b) FeMoNi model, (c) Differential charge density of FeMoNi model, wherein the blue contour indicated the charge accumulation, (d) Free energy diagram for intermediate adsorption, (e) The electron-localization function (ELF) of MoO_2 and FeMoNi. (f) PDOS diagram for oxygen's p orbital of MoO_2, FeMoNi and hydrogen's s orbital.

enhanced catalytic activity. As verification, we further explored the electrocatalytic activities (HER/OER) of FeMoNi/NF and FeMoNi/NF-C, which was performed as working electrode in alkaline seawater electrolyte. As expected, the FeMoNi/NF possessed a lower overpotential than FeMoNi/NF-C in term of HER/OER, as shown in Figs. S28a and S28b. The results aforementioned suggested that Joule heating played an important role as a profitable and facile method for the synthesis of high active electrocatalysts.

3.5. Density function theory (DFT) calculation

In order to probe the intrinsic catalytic mechanism of FeMoNi/NF for remarkable HER/OER performance, the DFT calculation was carried out. To investigate the electronic interactions provided by the synergistic effect of NiFe alloy and MoO_2 system, the PDOS of the correlative theoretical models (Fig. S29) were performed, as shown in the Fig. 8a and b. Compared with MoO_2, a higher density of carriers around the Fermi level was achieved for FeMoNi, confirming outstanding electrical conductivity and electron transfer rate [60], which benefited from the heterogeneous junction formed by NiFe alloy and MoO_2. For in-depth research of the effect of heterojunction, the differential charge density of FeMoNi model was calculated, wherein a zone of increased charge concentration was generated at NiFe alloy-MoO_2 interface (Fig. 8c), suggesting that more electron transfer was shifted from MoO_2 to the surface of the NiFe alloy during the reaction process, which is favorable to the increase of HER activity. Such result was also in agreement with electron transfer mentioned in the O 1 s and Ni 2p spectra (Fig. 2a, d). In addition, a low value of the hydrogen adsorption ability ΔG_{H^*} was essential for a glorious HER catalyst, which maintained a balance between the transfer of protons and separation of the adsorbed hydrogen [61,62]. As shown in the Fig. 8d, from a screening of the possible

catalytic sites on MoO_2 (Fig. S30) and FeMoNi model (Fig. S31), the ΔG_{H^*} value (0.06 eV) on FeMoNi was much better than MoO_2 (0.23 eV), which proved the rapid HER kinetics related with the enhanced HER activity of FeMoNi in the experiments. Interestingly, as depicted in Fig. 8d, the Mo site was the most reactive active site for the adsorption of H* on MoO_2, which was shifted to O sites on the FeMoNi model after the construction of heterogeneous junctions. In order to explore the active origin of O site, electron-localization function (ELF) maps of two different models were measured, wherein the electrons on O reactive sites of FeMoNi were more highly localized than MoO_2 (Fig. 8e), indicating the facilitated electrons transfer between H* intermediate and O sites. Meanwhile, the PDOS diagram for oxygen's p orbital of MoO_2 and FeMoNi were calculated, as shown in Fig. 8f. After the formation of the NiFe alloy and MoO_2 heterojunction, the p-orbital of oxygen was decreased and moved away from the s-orbital of hydrogen, which was characterized with reduced antibonding energy state and optimized the intermediate desorption [27]. Such result could also well explain the overly negative value at the O site (−0.80 eV) in MoO_2 and appropriate value at O site (0.06 eV) in FeMoNi. The above results showed that the NiFe alloy contact not only lead to tuning the electronic structure of catalyst but also decreasing the O 2p orbital of MoO_2, which accelerated the reaction kinetics for HER.

Besides, based on the above Raman, XRD and XPS results, the NiFe alloy would contribute to the surface reconstruction, which formed NiFe-hydroxide/MoO_2 heterojunction by in-situ generation of NiFe hydroxides on the surface of MoO_2 during the OER process. The enhanced OER activity was investigated by the DFT calculation, wherein the four steps of OER on (Ni, Fe)OOH/MoO_2 was showed in the Fig. 9a. For comparison, the free energy diagrams (U = 0) of reaction intermediates (O*, OH* and OOH*) catalyzed by MoO_2, NiOOH/MoO_2, FeOOH/MoO_2 and (Ni, Fe)OOH/MoO_2 were depicted in the Fig. 9b. Firstly, as shown in
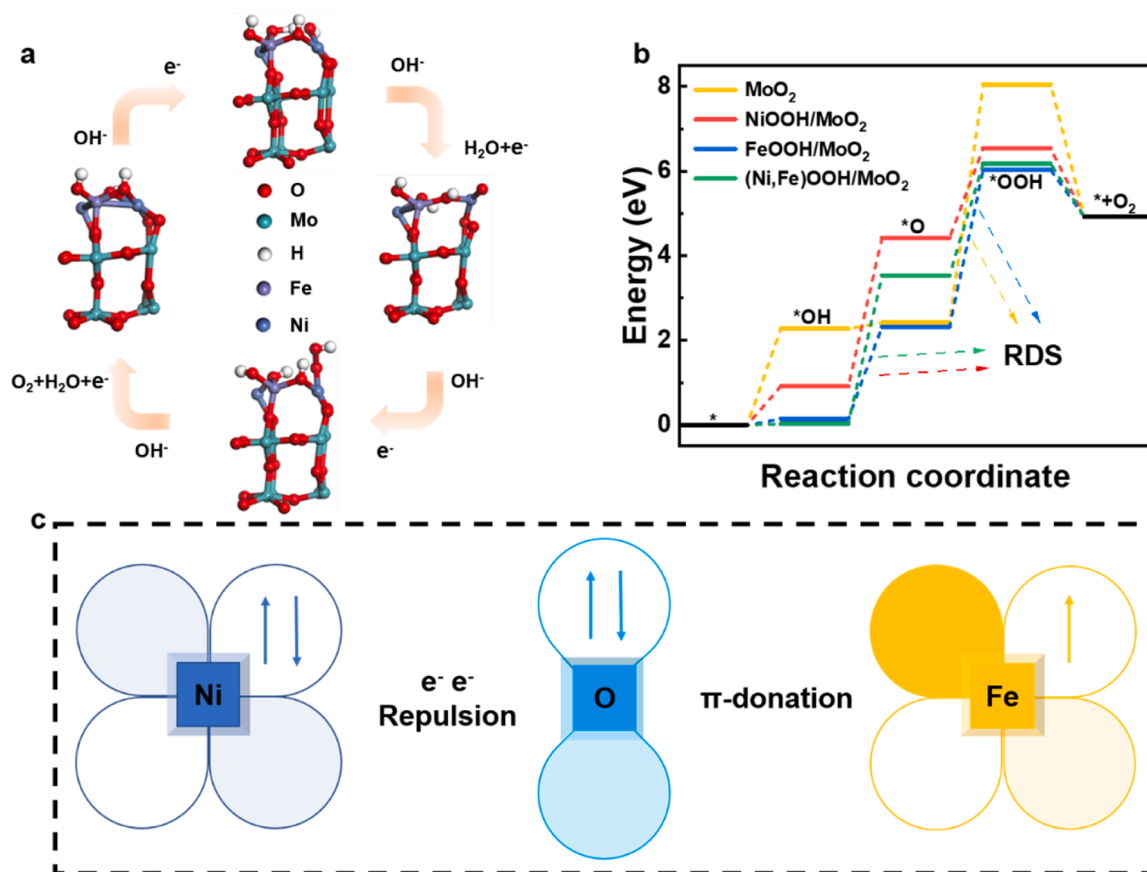

Fig. 9. (a) Schematic illustration of OER process on (Ni,Fe)OOH/MoO_2, (b) Free energy diagram for O, OH and OOH adsorptions in OER on MoO_2, NiOOH/MoO_2, FeOOH/MoO_2 and (Ni, Fe)OOH/MoO_2, (c)Schematic diagram of the electronic coupling between Ni and Fe in (Ni,Fe)OOH/MoO_2.

Table S5, it was deduced that the formation of heterojunction was more beneficial to the OER process comparing with MoO_2, in which the RDS for MoO_2 was $O^* \rightarrow OOH^*$ step and the ΔG value (5.631 eV) was much larger than those of other catalysts. The computational results demonstrated that the in-situ formed heterojunction could efficiently moderate the reaction energy barrier of RDS. Moreover, it should be noted that the RDS of $(Ni, Fe)OOH/MoO_2$ was $OH^* \rightarrow O^*$ step with a lower ΔG value (3.505 eV) than that of RDS in $NiOOH/MoO_2$ and $FeOOH/MoO_2$. It was most likely due to that the in-situ transformation of Fe^0 to Fe^{3+} could form unpaired electrons, which was in π-symmetry (t_{2g}) D-orbitals, thus leading to weaker electron interplay with O [63]. Conversely, the formed Ni^{3+} was characterized with totally occupied π-symmetry (t_{2g}) D-orbitals and more inclined to generate strong e^--e^- repulsion with O, which was favorable for synergistically electronic interaction between Ni and Fe (Fig. 9c) after the in-situ produced NiFe hydroxides, proving the enhanced OER activity of FeMoNi/NF than MoNi/NF [31] and FeMo/NF in theoretical calculation and experiments.

3.6. Overall water electrolysis

Inspired by the outstanding HER/OER performance, the overall water splitting (OWS) performance of FeMoNi/NF in 1 M alkaline seawater electrolyte was investigated as shown in the inset image of Fig. 10a. Unexpectedly, the assembled FeMoNi/NF(+)//FeMoNi/NF(-)

in a two-electrode configuration was performed, which only required a voltage of 1.48 V at the current density of 10 mA cm^{-2} and outperformed commercial RuO_2(+)//Pt/C(-) pair (1.60 V) (Fig. 10a). Such excellent OWS activity illustrated the promising application of FeMoNi/NF as an active and cost effective electrocatalyst in seawater. Besides, the FeMoNi/NF(+)//FeMoNi/NF(-) OWS system was continuously tested for 18 h at 250 mA cm^{-2}, and the performance was negligibly changed (Fig. 10b), which indicated the high feasibility of this materials for practical application. For comparison, the RuO_2(+)//Pt/C(-) OWS system exhibited extremely poor stability, due to the severe catalyst exfoliation and anodic corrosion under alkaline seawater conditions. In addition, Faradaic efficiency has been considered as an intuitive parameter for the catalyst performance, which could be calculated by drainage method as shown in the Fig. 10c. The generated gas volume of H_2 and O_2 bubbles were measured per 3 min, wherein the H_2/O_2 ratio was 2:1 and consistent with theoretical value, indicating as ~100 % Faradaic efficiency (Fig. 10d).

To further explore the potential of the commercial application, we evaluated the OWS activity in a MEA electrochemical reactor, as shown in Fig. 11a and Fig. S32. Typically, such assembled reactor (Fig. 11b) was applied in 1 M alkaline seawater included 2 cm * 2 cm anion exchange membrane (FAA-3-50) between two pieces FeMoNi/NF catalysts to prevented the confusion of H_2 and O_2. As shown in Fig. 11c, the FeMoNi/NF(+)//FeMoNi/NF(-) OWS system possessed the lowest cell
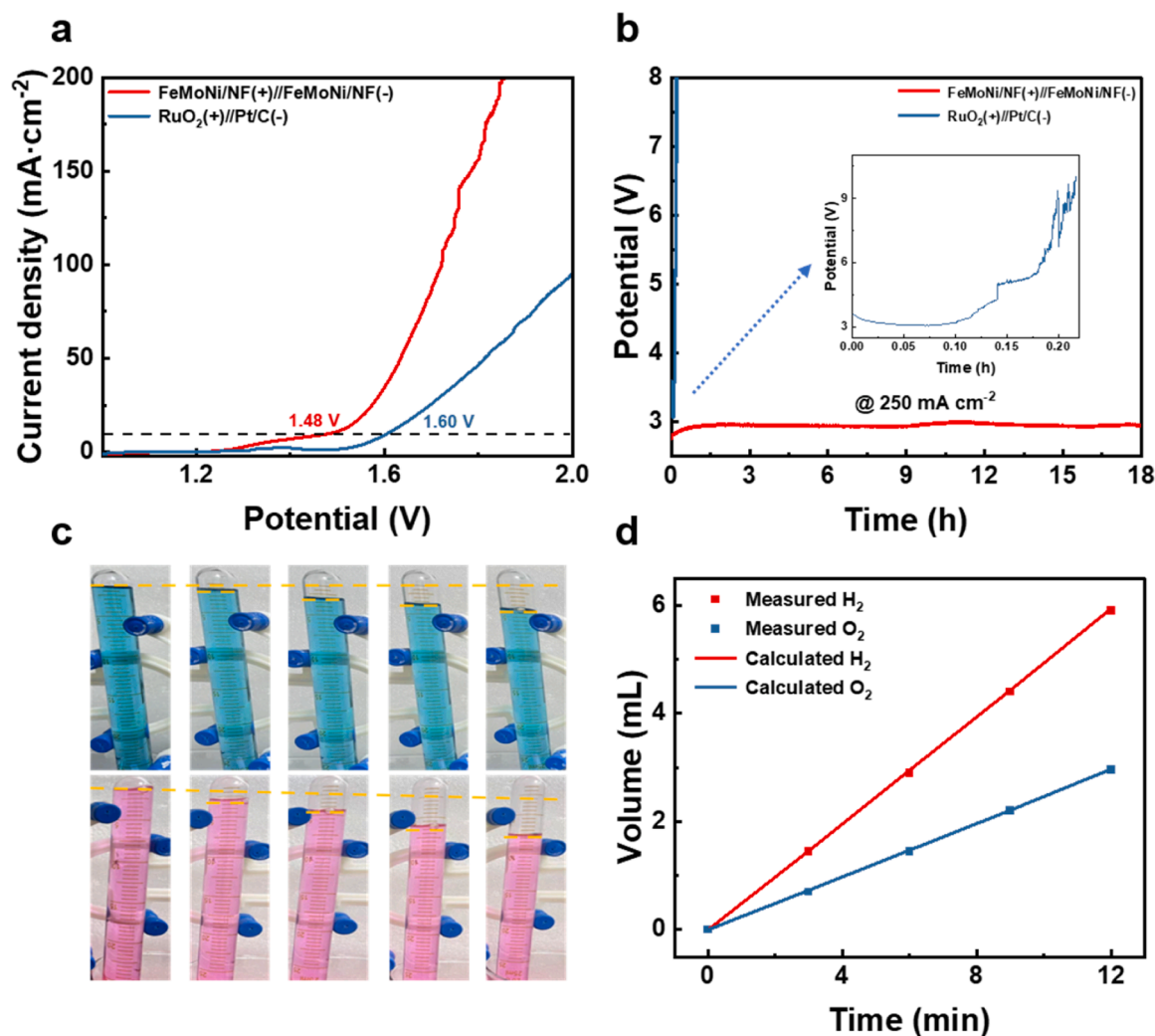

Fig. 10. (a) LSV curves in 1 M alkaline seawater electrolyte wherein the inset image was the measured electrolyzer, (b) Chronopotentiometry at 250 mA cm^{-2} of FeMoNi/NF(+)//FeMoNi/NF(-) and RuO_2(+)//Pt/C(-) in alkaline seawater electrolyte, (c) Photographs of H_2 (pink) and O_2 (blue) collected per 3 min, (d) The amount of calculated and measured H_2 and O_2 per 3 min.
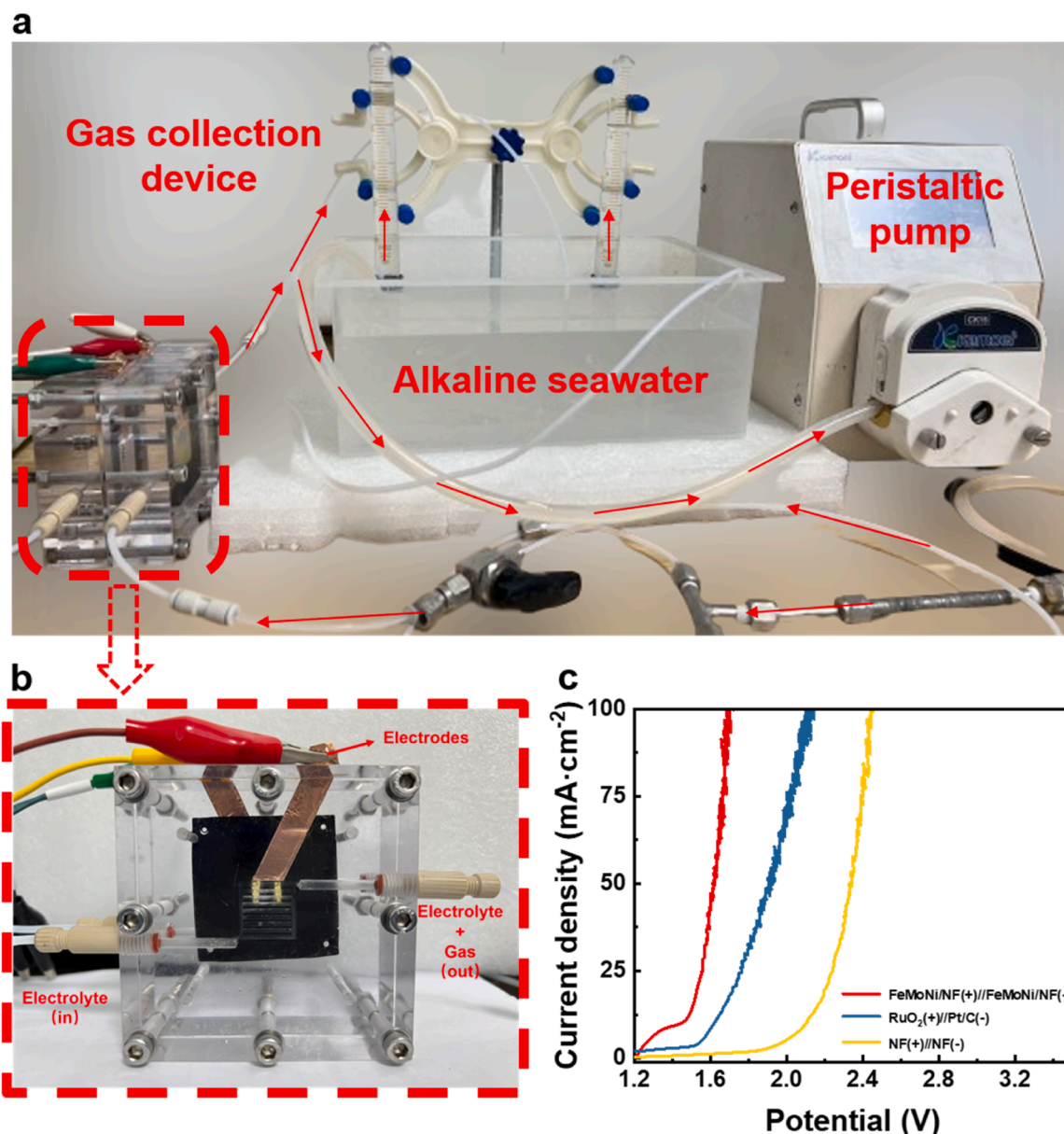
Fig. 11. (a, b) Schematic diagram of the MEA electrolyzer, (c) LSV curves without IR compensation measured in MEA electrolyzer among 1 M alkaline seawater electrolyte.

voltage (1.45 V) at 10 mA cm^{-2} (without IR compensation) much superior to the unit with RuO$_2$(+)//Pt/C(-) (1.62 V) and NF(+)//NF(-) (2.10 V). Moreover, it was worth noting that FeMoNi/NF(+)//FeMoNi/NF(-) possessed almost the same LSV curves at different flow rates, while the RuO$_2$(+)//Pt/C(-) system showed decreased OWS performance at lower flow rate, indicating enhanced transfer of electrolyte and hydrogen gas bubbles for FeMoNi/NF (Fig. S33). Besides, the associated energy consumption was evaluated at 100 mA cm^{-2} to further reflect the supremacy of FeMoNi/NF for commercial application. Fig. S34 and Table S6 showed that the FeMoNi/NF(+)//FeMoNi/NF(-) owned the lowest energy consumption (6.47 kW·h/m^3), which was promising for potential commercialization in seawater.

The PV-assisted water electrolysis system, as self-motivated electrolyzer driven by the inexpensive solar cells, has been considered as attractive way to cost-effectively generate hydrogen in recent years [64], which was restricted by the low STH efficiency (< 10 %). In order to reflect the superiority of FeMoNi/NF, a PV-assisted water electrolysis system was applied, which paired FeMoNi/NF(+)//FeMoNi/NF(-) and

tandem PSCs in alkaline seawater electrolyte. Typically, our home-made PSC realized solar-to-electric power conversion efficiency of ~16 % under simulated sunlight (AM 1.5 G), which achieved the open circuit voltage of 1.68 V and short-circuit current density of 13.9 mA cm^{-2} (Fig. 12a). The theoretical operation current density of PV-assisted water electrolysis system was reflected by the intersection point of I-V curves of tandem PSCs and FeMoNi/NF(+)//FeMoNi/NF(-) OWS, which provided a value of 10.15 mA·cm^{-2} corresponded to significantly high STH of 12.47 %. In addition, the transient photocurrent response measurement of PV-assisted water electrolysis system was carried out as shown in Fig. 12b, which could instantaneously reach the operating current, showing excellent light-driven reliability of such system. Meanwhile, our integrated system exhibited good long-term stability over 700 s without obvious operating current density and STH decay (Fig. 12c). Furthermore, the commercial silicon solar cell was also coupled with the two-electrode configuration to prove the possibility of practical application, which was well applied to simulated sun illumination (Fig. 12d) and outdoor sunshine (Fig. S35a) with visible bubbles
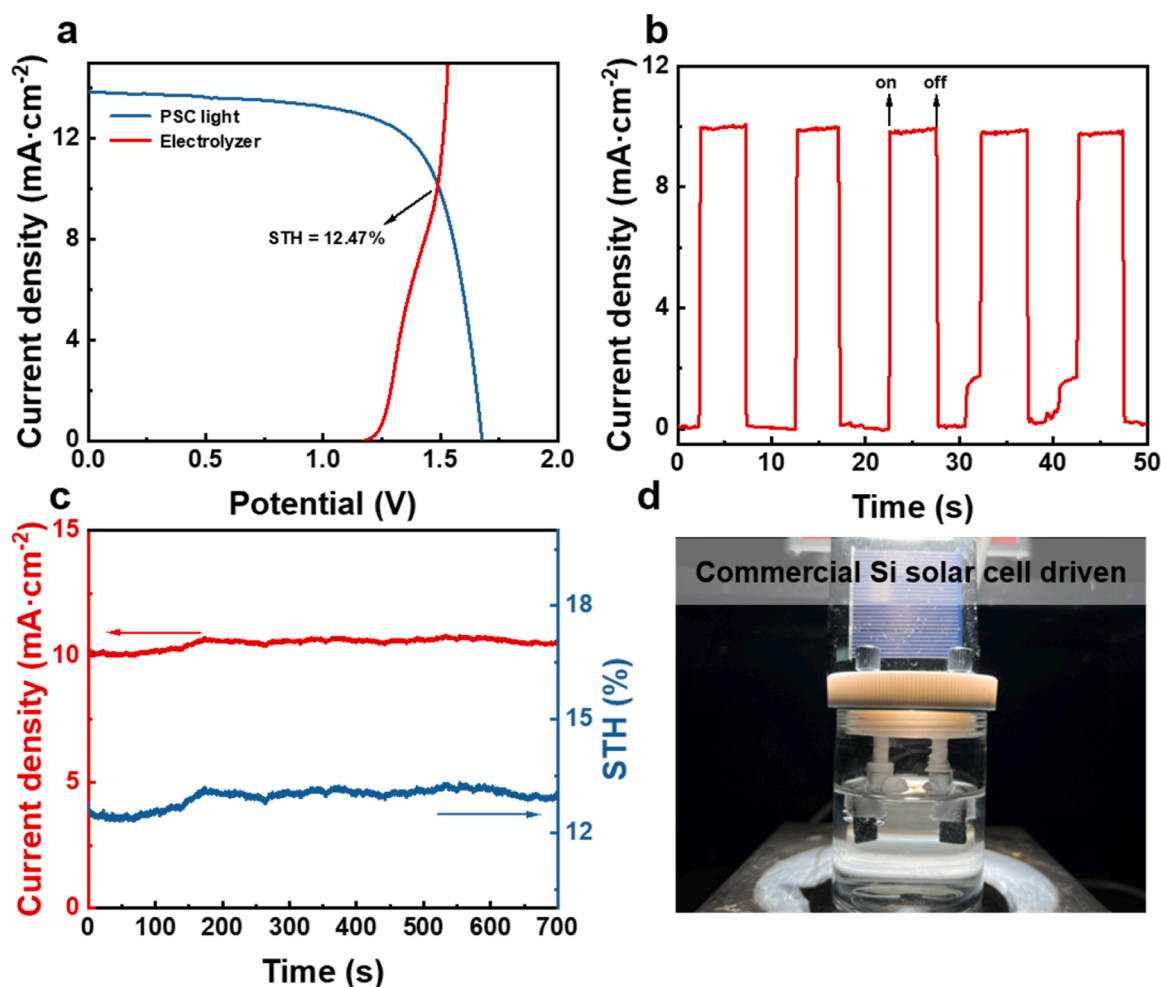
Fig. 12. (a) Current density–potential curves of tandem PSCs under simulated sun (AM 1.5-G 100 mW·cm^{-2}) illumination and FeMoNi/NF(+)//FeMoNi/NF(-) for overall water splitting in alkaline seawater electrolyte, (b) Instantaneous photocurrent response of solar-powered system, (c) Actual operating current density and calculated STH efficiency of solar power-assisted water splitting device, (d) Schematic illustration of a two-electrode configuration driven by the commercial silicon solar cell under simulated sun illumination.

(Fig. S35b). The above results manifested that the PV-assisted water electrolysis system with FeMoNi/NF was capable of satisfying the largescale commercialization of clean energy conversion.

4. Conclusions

In summary, we constructed a NiFe-MoO$_2$ heterostructure on Ni foam substrate (FeMoNi/NF) as highly efficient bifunctional electrocatalyst via rapid Joule heating. Such FeMoNi/NF electrocatalysts not only exhibited excellent HER/OER activity in alkaline seawater with low overpotential of 20 (250) mV at 10 (50) mA cm^{-2} but also showed outstanding long-term stability for high current density of 50, 250, 500 mA cm^{-2}. The as-prepared FeMoNi/NF integrated the merits of nanorod arrays with large specific surface areas and interface engineering, which exhibited remarkable electrocatalytic activities of HER/OER in alkaline seawater. Meanwhile, during the rapid heating/cooling process, the FeMoNi/NF exhibited face-centered cubic phase for Fe$_{0.5}$Ni$_{0.5}$ alloy and could further optimize the Fe-Ni bonds, electrical conductivity and achieve more O defects, causing better electrochemical properties than FeMoNi/NF-C (synthesized by CVD). Typically, the coupled FeMoNi/NF(+)//FeMoNi/NF(-) among MEA electrochemical reactor owned only 1.45 V at 10 mA·cm^{-2} and the lowest energy consumption (6.47 kW·h/m^3), which was promising for potential commercialization in seawater. Finally, a self-powered PV-assisted water electrolysis system with FeMoNi/NF was constructed and

represented a significant 12.47 % STH efficiency with good stability, which provides the possibility of carbon-free hydrogen production in the future.

CRediT authorship contribution statement

Zhan Zhao: Conceptualization, Methodology, Investigation, Writing – original draft, Writing – review & editing. **Jianpeng Sun:** Methodology, Investigation. **Xiang Li:** Methodology, Investigation. **Zisheng Zhang:** Methodology, Investigation, Writing – review & editing. **Xiangchao Meng:** Supervision, Conceptualization, Writing – original draft, Writing – review & editing.

Declaration of Competing Interest

The authors declare that they have no known competing financial interests or personal relationships that could have appeared to influence the work reported in this paper.

Data availability

Data will be made available on request.

Acknowledgements

X.M. acknowledges the financial supports from Taishan Scholars Foundation of Shandong Province (No.: tsqn201909058) and National Natural Science Foundation of China (Grant No: 22002146).

Appendix A. Supporting information

Supplementary data associated with this article can be found in the online version at doi:10.1016/j.apcatb.2023.123277.

References

[1] X. Tao, H. Xu, S. Luo, Y. Wu, C. Tian, X. Lu, Y. Qing, Construction of N-doped carbon nanotube encapsulated active nanoparticles in hierarchically porous carbonized wood frameworks to boost the oxygen evolution reaction, Appl. Catal. B Environ. 279 (2020) 119367–119376, https://doi.org/10.1016/j.apcatb.2020.119367.

[2] Z. Wang, W. Liu, Y. Hu, M. Guan, L. Xu, H. Li, J. Bao, H. Li, Cr-doped CoFe layered double hydroxides: highly efficient and robust bifunctional electrocatalyst for the oxidation of water and urea, Appl. Catal. B Environ. 272 (2020) 118959–118967, https://doi.org/10.1016/j.apcatb.2020.118959.

[3] M. Li, X. Wang, K. Liu, H. Sun, D. Sun, K. Huang, Y. Tang, W. Xing, H. Li, G. Fu, Reinforcing Co-O covalency via Ce(4f) horizontal line O(2p) horizontal line Co(3d) gradient orbital coupling for High-efficiency oxygen evolution, Adv. Mater. 35 (2023) 2302462–2302475, https://doi.org/10.1002/adma.202302462.

[4] Y. Zhu, X. Wang, X. Zhu, Z. Wu, D. Zhao, F. Wang, D. Sun, Y. Tang, H. Li, G. Fu, Improving the oxygen evolution activity of layered Double-hydroxide via Erbium-induced electronic coupling, Small 19 (2023) 2206531–2206541, https://doi.org/10.1002/smll.202206531.

[5] D. Wang, X. Jiang, Z. Lin, X. Zeng, Y. Zhu, Y. Wang, M. Gong, Y. Tang, G. Fu, Ethanol-induced hydrogen insertion in ultrafine IrPdH boosts pH-Universal hydrogen evolution, Small 18 (2022) 2204063–2204073, https://doi.org/10.1002/smll.202204063.

[6] Z. Zhao, J. Sun, X. Meng, Recent advances in transition metal-based electrocatalysts for seawater electrolysis, Int. J. Energy Res. 46 (2022) 17952–17975, https://doi.org/10.1002/er.8486.

[7] W. Tong, M. Forster, F. Dionigi, S. Dresp, R. Sadeghi Erami, P. Strasser, A.J. Cowan, P. Farràs, Electrolysis of low-grade and saline surface water, Nat. Energy 5 (2020) 367–377, https://doi.org/10.1038/s41560-020-0550-8.

[8] J.N. Hausmann, R. Schlögl, P.W. Menezes, M. Driess, Is direct seawater splitting economically meaningful? Energy Environ. Sci. 14 (2021) 3679–3685, https://doi.org/10.1039/d0ee03659e.

[9] S. Dresp, F. Dionigi, M. Klingenhof, P. Strasser, Direct electrolytic splitting of seawater: opportunities and challenges, ACS Energy Lett. 4 (2019) 933–942, https://doi.org/10.1021/acsenergylett.9b00220.

[10] J. Sun, S. Qin, X. Meng, Joule heating-induced synthesis of Co-NC electrocatalyst for hydrogen evolution reactionin seawater splitting, J. Liaocheng Univ. 36 (2023) 27–32, https://doi.org/10.19728/j.issn1672-6634.2023010012.

[11] J.-P. Sun, Z. Zhao, J. Li, Z.-Z. Li, X.-C. Meng, Recent advances in electrocatalytic seawater splitting, Rare Met. 42 (2022) 751–768, https://doi.org/10.1007/s12598-022-02168-x.

[12] J. Li, J. Sun, X. Meng, Spherical Co/Co₉S₈ as electrocatalyst for hydrogen production from alkaline solution and alkaline seawater, Int. J. Hydrog. Energy (2023), https://doi.org/10.1016/j.ijhydene.2023.04.175.

[13] R. Zhang, L. Wang, L. Pan, Z. Chen, W. Jia, X. Zhang, J.-J. Zou, Solid-acid-mediated electronic structure regulation of electrocatalysts and scaling relation breaking of oxygen evolution reaction, Appl. Catal. B Environ. 277 (2020) 119237–119245, https://doi.org/10.1016/j.apcatb.2020.119237.

[14] J. Sun, Z. Zhang, X. Meng, Low-Pt supported on MOF-derived Ni(OH)₂ with highly-efficiently electrocatalytic seawater splitting at high current density, Appl. Catal. B Environ. 331 (2023) 122703–122713, https://doi.org/10.1016/j.apcatb.2023.122703.

[15] J. Sun, Z. Zhao, J. Li, Z. Li, X. Meng, Recent advances in transition metal selenides-based electrocatalysts: rational design and applications in water splitting, J. Alloy. Compd. 918 (2022) 165719–165737, https://doi.org/10.1016/j.jallcom.2022.165719.

[16] G. Zhang, J. Zeng, J. Yin, C. Zuo, P. Wen, H. Chen, Y. Qiu, Iron-facilitated surface reconstruction to in-situ generate nickel–iron oxyhydroxide on self-supported FeNi alloy fiber paper for efficient oxygen evolution reaction, Appl. Catal. B Environ. 286 (2021) 119902–119913, https://doi.org/10.1016/j.apcatb.2021.119902.

[17] Z. Wang, J. Ang, J. Liu, X.Y.D. Ma, J. Kong, Y. Zhang, T. Yan, X. Lu, FeNi alloys encapsulated in N-doped CNTs-tangled porous carbon fibers as highly efficient and durable bifunctional oxygen electrocatalyst for rechargeable zinc-air battery, Appl. Catal. B Environ. 263 (2020) 118344–118356, https://doi.org/10.1016/j.apcatb.2019.118344.

[18] C. Wang, H. Yang, Y. Zhang, Q. Wang, NiFe alloy nanoparticles with hcp crystal structure stimulate superior oxygen evolution reaction electrocatalytic activity, Angew. Chem. Int Ed. Engl. 58 (2019) 6099–6103, https://doi.org/10.1002/anie.201902446.

[19] H. Fang, J. Yang, M. Wen, Q. Wu, Nanoalloy materials for chemical catalysis, Adv. Mater. 30 (2018), e1705698, https://doi.org/10.1002/adma.201705698.

[20] J.-J. Zhou, H. Ding, Z. Hua, L. Xu, W. Wang, L. Wang, L. Han, L. Chen, Unveiling high intrinsic activity of Co₃Mo alloy and metallic Ni embedded in CoNiMo-O nanosheets arrays for hydrogen evolution reaction, Chem. Eng. J. 450 (2022) 138206–138216, https://doi.org/10.1016/j.cej.2022.138206.

[21] L. Shang, Y. Zhao, X.-Y. Kong, R. Shi, G.I. Waterhouse, L. Wen, T. Zhang, Underwater superaerophobic Ni nanoparticle-decorated nickel–molybdenum nitride nanowire arrays for hydrogen evolution in neutral media, Nano Energy 78 (2020) 105375–105382, https://doi.org/10.1016/j.nanoen.2020.105375.

[22] L. Peng, C. Wang, Q. Wang, R. Shi, T. Zhang, G.I. Waterhouse, Rationally designed Ni–Ni₃S₂ interfaces for efficient overall water electrolysis, Adv. Energy Sustain. Res. 2 (2021) 2100078–2100085, https://doi.org/10.1002/aesr.202100078.

[23] Y. Niu, X. Teng, S. Gong, Z. Chen, A bimetallic alloy anchored on biomass-derived porous N-doped carbon fibers as a self-supporting bifunctional oxygen electrocatalyst for flexible Zn–air batteries, J. Mater. Chem. A 8 (2020) 13725–13734, https://doi.org/10.1039/d0ta03288c.

[24] Z. Li, X. Wu, X. Jiang, B. Shen, Z. Teng, D. Sun, G. Fu, Y. Tang, Surface carbon layer controllable Ni₃Fe particles confined in hierarchical N-doped carbon framework boosting oxygen evolution reaction, Adv. Powder Mater. 1 (2022) 100020–100031, https://doi.org/10.1016/j.apmate.2021.11.007.

[25] Q. Hu, X. Liu, B. Zhu, L. Fan, X. Chai, Q. Zhang, J. Liu, C. He, Z. Lin, Crafting MoC₂-doped bimetallic alloy nanoparticles encapsulated within N-doped graphene as roust bifunctional electrocatalysts for overall water splitting, Nano Energy 50 (2018) 212–219, https://doi.org/10.1016/j.nanoen.2018.05.033.

[26] S. Fu, J. Song, C. Zhu, G.-L. Xu, K. Amine, C. Sun, X. Li, M.H. Engelhard, D. Du, Y. Lin, Ultrafine and highly disordered Ni₂Fe₁ nanofoams enabled highly efficient oxygen evolution reaction in alkaline electrolyte, Nano Energy 44 (2018) 319–326, https://doi.org/10.1016/j.nanoen.2017.12.010.

[27] X. Liu, K. Ni, C. Niu, R. Guo, W. Xi, Z. Wang, J. Meng, J. Li, Y. Zhu, P. Wu, Q. Li, J. Luo, X. Wu, L. Mai, Upraising the O 2p orbital by integrating Ni with MoO₂ for accelerating hydrogen evolution kinetics, ACS Catal. 9 (2019) 2275–2285, https://doi.org/10.1021/acscatal.8b04817.

[28] Y.Y. Chen, Y. Zhang, X. Zhang, T. Tang, H. Luo, S. Niu, Z.H. Dai, L.J. Wan, J.S. Hu, Self-templated fabrication of MoNi₄/MoO₃₋ₓ nanorod arrays with dual active components for highly efficient hydrogen evolution, Adv. Mater. 29 (2017) 1703311–1703318, https://doi.org/10.1002/adma.201703311.

[29] G.H. Han, H. Kim, J. Kim, J. Kim, S.Y. Kim, S.H. Ahn, Micro-nanoporous MoO₂@CoMo heterostructure catalyst for hydrogen evolution reaction, Appl. Catal. B Environ. 270 (2020) 118895–118905, https://doi.org/10.1016/j.apcatb.2020.118895.

[30] H. Huang, S. Zhou, C. Yu, H. Huang, J. Zhao, L. Dai, J. Qiu, Rapid and energy-efficient microwave pyrolysis for high-yield production of highly-active bifunctional electrocatalysts for water splitting, Energy Environ. Sci. 13 (2020) 545–553, https://doi.org/10.1039/c9ee03273h.

[31] Z. Zhao, J. Sun, Z. Li, X. Xu, Z. Zhang, C. Li, L. Wang, X. Meng, Rapid synthesis of efficient Mo-based electrocatalyst for the hydrogen evolution reaction in alkaline seawater with 11.28% solar-to-hydrogen efficiency, J. Mater. Chem. A 11 (2023) 10346–10359, https://doi.org/10.1039/d3ta01522j.

[32] G. Kresse, J. Furthmuller, Efficiency of ab-initio total energy calculations for metals and semiconductors using a plane-wave basis set, Comp. Mater. Sci. 6 (1996) 15–50, https://doi.org/Doi 10.1016/0927-0256(96)00008-0.

[33] J.P. Perdew, J.A. Chevary, S.H. Vosko, K.A. Jackson, M.R. Pederson, D.J. Singh, C. Fiolhais, Atoms, molecules, solids, and surfaces: applications of the generalized gradient approximation for exchange and correlation, Phys. Rev. B 46 (1992) 6671–6687, https://doi.org/10.1103/physrevb.46.6671.

[34] Z. Xiao, M. Yang, J. Wang, Z. Xu, S. Zhang, A. Tang, R. Gao, H. Yang, FeNiP/MoOx integrated electrode grown on monocrystalline NiMoO₄ nanorods with multi-interface for accelerating alkaline hydrogen evolution reaction, Appl. Catal. B Environ. 303 (2022) 120913–120921, https://doi.org/10.1016/j.apcatb.2021.120913.

[35] F. Yang, Y. Luo, Q. Yu, Z. Zhang, S. Zhang, Z. Liu, W. Ren, H.M. Cheng, J. Li, B. Liu, A durable and efficient electrocatalyst for saline water splitting with current density exceeding 2000 mA cm⁻², Adv. Funct. Mater. 31 (2021) 2010367–2010377, https://doi.org/10.1002/adfm.202010367.

[36] S. Crouch-Baker, P.G. Dickens, Standard molar enthalpies of formation of MoO₃·2H₂O and yellow MoO₃·H₂O by solution calorimetry, J. Chem. Thermodyn. 15 (1983) 675–679, https://doi.org/10.1016/0021-9614(83)90081-2.

[37] K. Dastafkan, Q. Meyer, X. Chen, C. Zhao, Efficient oxygen evolution and gas bubble release achieved by a low gas bubble adhesive iron-nickel vanadate electrocatalyst, Small 16 (2020) 2002412–2022424, https://doi.org/10.1002/smll.202002412.

[38] C. Niu, X. Liu, J. Meng, L. Xu, M. Yan, X. Wang, G. Zhang, Z. Liu, X. Xu, L. Mai, Three dimensional V₂O₅/NaV₆O₁₅ hierarchical heterostructures: controlled synthesis and synergistic effect investigated by in situ X-ray diffraction, Nano Energy 27 (2016) 147–156, https://doi.org/10.1016/j.nanoen.2016.06.057.

[39] B. Lin, J. Chen, R. Yang, S. Mao, M. Qin, Y. Wang, Multi-hierarchical cobalt-based electrocatalyst towards high rate H₂ production, Appl. Catal. B Environ. 316 (2022) 121666–121678, https://doi.org/10.1016/j.apcatb.2022.121666.

[40] F. Guo, Y. Wu, H. Chen, Y. Liu, L. Yang, X. Ai, X. Zou, High-performance oxygen evolution electrocatalysis by boronized metal sheets with self-functionalized surfaces, Energy Environ. Sci. 12 (2019) 684–692, https://doi.org/10.1039/c8ee03405b.

[41] R. Subbaraman, D. Tripkovic, K.-C. Chang, D. Strmcnik, A.P. Paulikas, P. Hirunsit, M. Chan, J. Greeley, V. Stamenkovic, N.M. Markovic, Trends in activity for the water electrolyser reactions on 3 d M (Ni, Co, Fe, Mn) hydr (oxy) oxide catalysts, Nat. Mater. 11 (2012) 550–557, https://doi.org/10.1038/nmat3313.

[42] X. Wang, R. Su, H. Aslan, J. Kibsgaard, S. Wendt, L. Meng, M. Dong, Y. Huang, F. Besenbacher, Tweaking the composition of NiMoZn alloy electrocatalyst for enhanced hydrogen evolution reaction performance, Nano Energy 12 (2015) 9–18, https://doi.org/10.1016/j.nanoen.2014.12.007.

[43] J.X. Feng, J.Q. Wu, Y.X. Tong, G.R. Li, Efficient hydrogen evolution on Cu Nanodots-decorated Ni_3S_2 nanotubes by optimizing atomic hydrogen adsorption and desorption, J. Am. Chem. Soc. 140 (2018) 610–617, https://doi.org/10.1021/jacs.7b08521.

[44] K.L. Zhou, Z. Wang, C.B. Han, X. Ke, C. Wang, Y. Jin, Q. Zhang, J. Liu, H. Wang, H. Yan, Platinum single-atom catalyst coupled with transition metal/metal oxide heterostructure for accelerating alkaline hydrogen evolution reaction, Nat. Commun. 12 (2021) 3783–3793, https://doi.org/10.1038/s41467-021-24079-8.

[45] J. Kibsgaard, T.F. Jaramillo, F. Besenbacher, Building an appropriate active-site motif into a hydrogen-evolution catalyst with thiomolybdate $[Mo_3S_{13}]^{2-}$ clusters, Nat. Chem. 6 (2014) 248–253, https://doi.org/10.1038/nchem.1853.

[46] J. Sun, F. Tian, F. Yu, Z. Yang, B. Yu, S. Chen, Z. Ren, H. Zhou, Robust Hydrogen-evolving electrocatalyst from heterogeneous molybdenum Disulfide-based catalyst, ACS Catal. 10 (2019) 1511–1519, https://doi.org/10.1021/acscatal.9b03030.

[47] Y. Yan, P. Gu, S. Zheng, M. Zheng, H. Pang, H. Xue, Facile synthesis of an accordion-like Ni-MOF superstructure for high-performance flexible supercapacitors, J. Mater. Chem. A 4 (2016) 19078–19085, https://doi.org/10.1039/c6ta08331e.

[48] M.B. Stevens, C.D.M. Trang, L.J. Enman, J. Deng, S.W. Boettcher, Reactive Fe-Sites in Ni/Fe (Oxy)hydroxide are responsible for exceptional oxygen electrocatalysis activity, J. Am. Chem. Soc. 139 (2017) 11361–11364, https://doi.org/10.1021/jacs.7b07117.

[49] L. Yang, H. Xu, H. Liu, D. Cheng, D. Cao, Active site identification and evaluation criteria of in situ grown CoTe and NiTe nanoarrays for hydrogen evolution and oxygen evolution reactions, Small Methods 3 (2019) 1900113–1900124, https://doi.org/10.1002/smtd.201900113.

[50] P. Liu, W. Pan, R. Yao, L. Zhang, Q. Wu, F. Kang, H.J. Fan, C. Yang, NiMoFe nanoparticles@MoO_2 nano-pillar arrays as bifunctional electrodes for ultra-low-voltage overall water splitting, J. Mater. Chem. A 10 (2022) 3760–3770, https://doi.org/10.1039/d1ta09245f.

[51] Y. Wang, Y. Zhu, S. Zhao, S. She, F. Zhang, Y. Chen, T. Williams, T. Gengenbach, L. Zu, H. Mao, W. Zhou, Z. Shao, H. Wang, J. Tang, D. Zhao, C. Selomulya, Anion etching for accessing rapid and deep Self-reconstruction of precatalysts for water oxidation, Matter 3 (2020) 2124–2137, https://doi.org/10.1016/j.matt.2020.09.016.

[52] W. Shi, J. Zhu, L. Gong, D. Feng, Q. Ma, J. Yu, H. Tang, Y. Zhao, S. Mu, Fe-Incorporated Ni/MoO_2 hollow heterostructure nanorod arrays for High-efficiency overall water splitting in alkaline and seawater media, Small 18 (2022) 2205683–2205692, https://doi.org/10.1002/smll.202205683.

[53] M. Legodi, D. Dewaal, The preparation of magnetite, goethite, hematite and maghemite of pigment quality from mill scale iron waste, Dyes Pigments 74 (2007) 161–168, https://doi.org/10.1016/j.dyepig.2006.01.038.

[54] L. Yu, Q. Zhu, S. Song, B. McElhenny, D. Wang, C. Wu, Z. Qin, J. Bao, Y. Yu, S. Chen, Z. Ren, Non-noble metal-nitride based electrocatalysts for high-performance alkaline seawater electrolysis, Nat. Commun. 10 (2019) 5106–5116, https://doi.org/10.1038/s41467-019-13092-7.

[55] H. Liao, X. Zhang, S. Niu, P. Tan, K. Chen, Y. Liu, G. Wang, M. Liu, J. Pan, Dynamic dissolution and re-adsorption of molybdate ion in iron incorporated nickel-molybdenum oxyhydroxide for promoting oxygen evolution reaction, Appl. Catal. B Environ. 307 (2022) 121150–121160, https://doi.org/10.1016/j.apcatb.2022.121150.

[56] F. Yu, H. Zhou, Y. Huang, J. Sun, F. Qin, J. Bao, W.A. Goddard 3rd, S. Chen, Z. Ren, High-performance bifunctional porous non-noble metal phosphide catalyst for overall water splitting, Nat. Commun. 9 (2018) 2551–2560, https://doi.org/10.1038/s41467-018-04746-z.

[57] X. Xu, F. Song, X. Hu, A nickel iron diselenide-derived efficient oxygen-evolution catalyst, Nat. Commun. 7 (2016) 12324–12331, https://doi.org/10.1038/ncomms12324.

[58] G. Xiong, Y. Chen, Z. Zhou, F. Liu, X. Liu, L. Yang, Q. Liu, Y. Sang, H. Liu, X. Zhang, J. Jia, W. Zhou, Rapid synthesis of various electrocatalysts on Ni foam using a universal and facile induction heating method for efficient water splitting, Adv. Funct. Mater. 31 (2021) 2009580–2009591, https://doi.org/10.1002/adfm.202009580.

[59] H. Cheng, N. Yang, Q. Lu, Z. Zhang, H. Zhang, Syntheses and properties of metal nanomaterials with novel crystal phases, Adv. Mater. 30 (2018) 1707189–1707212, https://doi.org/10.1002/adma.201707189.

[60] Y. Cheng, H. Guo, P. Yuan, X. Li, L. Zheng, R. Song, Self-supported bifunctional electrocatalysts with Ni nanoparticles encapsulated in vertical N-doped carbon nanotube for efficient overall water splitting, Chem. Eng. J. 413 (2021) 127531–127539, https://doi.org/10.1016/j.cej.2020.127531.

[61] P. Li, X. Duan, S. Wang, L. Zheng, Y. Li, H. Duan, Y. Kuang, X. Sun, Amorphous ruthenium-sulfide with isolated catalytic sites for Pt-like electrocatalytic hydrogen production over whole pH range, Small 15 (2019) 1904043–1904051, https://doi.org/10.1002/smll.201904043.

[62] J. Kibsgaard, C. Tsai, K. Chan, J.D. Benck, J.K. Nørskov, F. Abild-Pedersen, T. F. Jaramillo, Designing an improved transition metal phosphide catalyst for hydrogen evolution using experimental and theoretical trends, Energy Environ. Sci. 8 (2015) 3022–3029, https://doi.org/10.1039/c5ee02179k.

[63] C. Jia, C. Zhen, L. Yin, H. Zhu, P. Du, A. Han, G. Liu, H.-M. Cheng, Topologic transition-induced abundant undercoordinated Fe active sites in NiFeOOH for superior oxygen evolution, Nano Energy 106 (2023) 108044–108054, https://doi.org/10.1016/j.nanoen.2022.108044.

[64] R. Andaveh, A. Sabour Rouhaghdam, J. Ai, M. Maleki, K. Wang, A. Seif, G. Barati Darband, J. Li, Boosting the electrocatalytic activity of NiSe by introducing MnCo as an efficient heterostructured electrocatalyst for large-current-density alkaline seawater splitting, Appl. Catal. B Environ. 325 (2023) 122355–122369, https://doi.org/10.1016/j.apcatb.2022.122355.